

**Max-Planck-Institut  
für Mathematik  
in den Naturwissenschaften  
Leipzig**

**Scale Free Avalanches in  
Excitatory-Inhibitory Populations of  
Spiking Neurons with Conductance  
Based Synaptic Currents**

(revised version: April 2022)

by

*Masud Ehsani and Jürgen Jost*

Preprint no.: 13

2022





# Scale Free Avalanches in Excitatory-Inhibitory Populations of Spiking Neurons with Conductance Based Synaptic Currents

Masud Ehsani<sup>1\*</sup> and Jürgen Jost<sup>1,2</sup>

<sup>1\*</sup> Max Planck Institute for Mathematics in Sciences, Inselstr.22,  
Leipzig, 04103, Saxony, Germany .

<sup>2</sup>Santa Fe Institute, 1399 Hyde Park Rd, Santa Fe, NM 87501,  
United States .

\*Corresponding author(s). E-mail(s): [masud.ehsani@mis.mpg.de](mailto:masud.ehsani@mis.mpg.de);  
Contributing authors: [jjost@mis.mpg.de](mailto:jjost@mis.mpg.de);

## Abstract

We investigate spontaneous critical dynamics of excitatory and inhibitory (EI) sparsely connected populations of spiking leaky integrate-and-fire neurons with conductance-based synapses. We use a bottom-up approach to derive a single neuron gain function and a linear Poisson neuron approximation which we use to study mean-field dynamics of the EI population and its bifurcations. In the low firing rate regime, the quiescent state loses stability due to saddle-node or Hopf bifurcations. In particular, at the Bogdanov-Takens (BT) bifurcation point which is the intersection of the Hopf bifurcation and the saddle-node bifurcation lines of the 2D dynamical system, the network shows avalanche dynamics with power-law avalanche size and duration distributions. This matches the characteristics of low firing spontaneous activity in the cortex. By linearizing gain functions and excitatory and inhibitory nullclines, we can approximate the location of the BT bifurcation point. This point in the control parameter phase space corresponds to the internal balance of excitation and inhibition and a slight excess of external excitatory input to the excitatory population. Due to the tight balance of average excitation and inhibition currents, the firing of the individual cells is fluctuation-driven. Around the BT point, the spiking of neurons is a Poisson process and the population average membrane potential of neurons is approximately at the middle

of the operating interval  $[\mathbf{V}_{Rest}, \mathbf{V}_{th}]$ . Moreover, the EI network is close to both oscillatory and active-inactive phase transition regimes.

**Keywords:** Critical Brain Hypothesis, Scale Free Avalanches, Linear Poisson Neuron, Bogdanov-Takens Bifurcation

## 1 Introduction

Experiments have shown that in the absence of stimuli, the cortical population of neurons shows rich dynamical patterns, called spontaneous activity, which do not look random and entirely noise-driven but are structured in spatiotemporal patterns (Takeda et al (2016); Thompson et al (2014)). Spontaneous activity is assumed to be the substrate or background state of the neural system with functional significance (Raichle (2010)). Experimental findings on different temporal and spatial resolutions highlight the scale-free characteristic of spontaneous activity.

In microcircuits of the brain during spontaneous activity, we observe avalanche dynamics. This mode of activity was first closely investigated by Beggs and Plenz (2003) in cultured slices of rat cortex using a multi-electrode array with an inter-electrode distance of  $200\mu m$  to record local field potentials (LFP). An avalanche is defined as almost synchronized epochs of activity separated by usually long periods of inactivity. At higher temporal resolution this seemingly synchronized pattern appears as a cascade of activity in micro-electrodes arrays initiated from one (or a few) local sites that propagate through the network and finally terminate. The main finding of this seminal experimental paper is power-law scaling of the probability density function for size and duration of avalanches. And causing an excitation and inhibition imbalance by injecting specific drugs destroys power-law scaling. Further studies confirm these results in different setups like awake monkeys (Petermann et al (2009)), in the cerebral cortex and hippocampus of anesthetized, asleep, and awake rats (Ribeiro et al (2010)) and the visual cortex of an anesthetized cat (Hahn et al (2010)). Besides LFP data several studies report the scale-free avalanche size distribution based on spike data (Friedman et al (2012), Hahn et al (2010), Mazzoni et al (2007)). Friedman et al (2012) analyzed cultured slices of cortical tissue and collected data at individual neurons with different spacing. Klaus et al (2011) showed that a power law is the best fit for neural avalanches collected from in vivo and in vitro experiments.

Besides power-law scaling of size and duration of avalanches with exponents  $\tau \sim -1.5$  and  $\alpha \sim -2$ , respectively, they showed that the temporal profile of avalanches is described by a single universal scaling function. Average size versus average duration of avalanches is also a power-law with  $\langle s \rangle = \langle T \rangle \frac{1}{\sigma \nu z}$  linked by a scaling relation  $\frac{\alpha - 1}{\tau - 1} = \frac{1}{\sigma \nu z}$  between exponents. In addition,

the mean temporal profile of avalanches follows a scaling form as in non-equilibrium critical dynamics,

$$S(t, T) \sim T^{1/\sigma\nu z - 1} F(t/T) \quad (1)$$

Data sets collapse to the scaling function very well. The appearance of power laws, scaling relations among their exponents, data collapse, and sensitivity to the imbalance of excitation and inhibition led to the hypothesis that somehow the brain is poised near criticality by a self-organization mechanism with the balance of excitatory and inhibitory rates as the self-organizing parameter. In this direction, many models have been presented in the past decades. Short-term plasticity in excitatory neuronal models has been investigated as a self-organizing principle for a non-conservative neuronal model [Levina et al \(2009, 2007\)](#); [Peng and Beggs \(2013\)](#); [di Santo et al \(2018\)](#); [Brochini et al \(2016\)](#). In addition, self-organization by other control parameters like degree of connectivity or synaptic strength [Bornholdt and Roehl \(2003\)](#); [Rybarsch and Bornholdt \(2014\)](#), STDP [Meisel and Gross \(2009\)](#), and balanced input [Benayoun et al \(2010\)](#) has been studied.

On the other hand, the spontaneous firing of single neocortical neurons is considered to be a noisy, stochastic process resembling a Poisson point process. It has been claimed that the balance of excitation and inhibition is a necessary condition for the noisy irregular firing of individual neurons as well as scale free avalanche patterns at the population level. Since the network is settled in a balanced state, a small deviation in the balance condition leads to a local change in the firing rate. Therefore, the system is highly sensitive to input while maintaining a low firing rate and highly variable spike trains at the individual neuron level. Inhibitory-excitatory balance can lead to asynchronous cortical states in local populations ([Brunel and Hakim \(1999, 2000, 2008\)](#)) and the emergence of waves and fronts at a larger scale of cortical activity ([Ermentrout \(1998\)](#); [Bressloff \(2011\)](#)). At the level of individual neurons, this balance leads to highly irregular firing of neurons with inter-spike interval distribution with CV close to one and thus resembling a Poisson process ([Softky and Koch \(1993\)](#)). Studies using the voltage clamp method tracking conductance of excitatory and inhibitory synapses on neurons both in vivo and in vitro, confirmed that there exist proportionality and balance of inhibitory and excitatory currents during upstate ([Haider et al \(2006\)](#)), sensory input ([Shu et al \(2003\)](#)) and spontaneous activity ([Okun and Lampl \(2008\)](#)). [Benayoun et al \(2010\)](#) proposed a stochastic model of spiking neurons which matches the Wilson-Cowan mean field in the limit of infinite system size that shows scale-free avalanches in the balanced state in which sum of excitation and inhibition is much larger than the net difference between them. Under symmetry condition on weights this makes the Jacobian to have two negative eigenvalues close to zero in the balanced state suggesting the system operating in the vicinity of a Bogdanov-Takens bifurcation point. [Cowan et al \(2013\)](#) used the method of path integral representation in the stochastic model of spiking neurons supplemented by anti-Hebbian synaptic plasticity as the self-organizing mechanism.

Their network possesses bistability close to the saddle-node bifurcation point which is the origin of the avalanche behavior in the system.

In this work, we start from a bottom-up approach by analytically investigating conditions on Poisson firing at the single neuron level and introducing conditions on the balance of inhibitory and excitatory currents. Poisson firing condition has been studied before in integrate and fire neurons with non-conductance based and only excitatory current (Kistler and van Hemmen (2000)). Here, we investigate conditions on balanced conductance-based input currents that lead to Poisson firing. Next, we build a linear Poisson neuron model with minimal error in the low firing rate regime. The linear Poisson regime of firing is a segment of the dynamical regime of the neuron response. We can use this linearization to form an approximate linearized gain function. This gain function can then be used to investigate dynamics of a sparsely or all to all connected homogeneous network of inhibitory and excitatory neurons and its bifurcation diagram. We also introduce another compatible approximation of gain functions by sigmoids. We observe avalanche patterns with power-law distributed sizes and duration at the intersection of saddle-node and Hopf bifurcation lines, i.e., at a Bogdanov-Takens (BT) bifurcation point of the mean field equations. At this point, the balance of excitatory and inhibitory inputs leads to stationary values of membrane potentials that allow Poisson firing at the single neuron level and avalanche type dynamics at the population level. The firing of neurons is due to the accumulation of internal currents, and external input by itself does not suffice to trigger firing. However, external input imbalance to excitatory and inhibitory populations is needed for the initiation of the avalanche. During each avalanche at the BT point, each neuron on average activates one another neuron which leads to termination of avalanches with power-law distributed durations and sizes. This is the case when currents to single cells are balanced in a way that excess excitation firing is compensated by inhibitory feedback. A linear relation between excitatory and inhibitory rates close to the BT point enables us to write down the dynamics of the excitatory population as a branching process. Close to the BT point the branching parameter is close to one which is indicative of the critical state. Tuning the system at BT can be attained by a balance of inhibitory feedback leading to a condition on synaptic weights and adjustment of excess external drive to the excitatory population. This is investigated in another article (Ehsani and Jost (2022)), where we show how learning by STDP and homeostatic synaptic plasticity as self-organizing principles can tune the system close to the BT point by regulating the inhibitory feedback strength and excitatory population gain.

## 2 Neuron model and network architecture

We use an integrate and fire neuron model in which the change in the membrane voltage of the neuron receiving time dependent synaptic current  $i(t)$

follows :

$$C \frac{dv(t)}{dt} = g_{Leak}(v_{Leak} - v(t)) + i(t), \quad (2)$$

for  $v(t) < v_{th}$ . When the membrane voltage reaches  $v_{th} = -50mv$ , the neuron spikes and immediately its membrane voltage resets to  $v_{rest}$  which is equal to  $v_{Leak} = -65mv$ .

In the following, we want to concentrate on a model with just one type of inhibitory and one type of excitatory synapses, which can be seen as the average effect of the two types of synapses. We can write the synaptic inhibitory and excitatory current as

$$i(t) = g_{inh}(t) * (V_{Rinh} - v(t)) + g_{exc}(t) * (V_{Rexc} - v(t)) \quad (3)$$

$V_{Rinh}$  and  $V_{Rexc}$  are the reverse potentials of excitatory and inhibitory ion channels, and based on experimental studies we choose values of  $-80mv$  and  $0mv$  for them respectively.  $g_{inh}(t)$  and  $g_{exc}(t)$  are the conductances of inhibitory and excitatory ion channels. These conductances are changing by the inhibitory and excitatory input to the cell. Each spike of a presynaptic inhibitory or excitatory neuron  $j$  to a postsynaptic neuron  $k$  that is received by  $k$  at time  $t_0$  will change the inhibitory or excitatory ion channel conductance of the postsynaptic neuron for  $t > t_0$  according to

$$\begin{aligned} g_{Inh}^k(t) &= w_{kj} * g_0^{inh} * \exp\left(-\frac{t - t_0}{\tau_{syn}^{inh}}\right) \\ g_{Exc}^k(t) &= w_{kj} * g_0^{exc} * \exp\left(-\frac{t - t_0}{\tau_{syn}^{exc}}\right) \end{aligned} \quad (4)$$

Here we assume that the rise time of synaptic conductances is very small compared to other time scales in the model and therefore, we modeled the synaptic current by a decay term with synaptic decay time constant  $\tau_{syn}$  which we assume to be the same value of  $5ms$  for both inhibitory and excitatory synapses. In the remainder of this work, in the simulation, we consider a population of  $N_{Exc} = 2 * 10^4$  and  $N_{Inh} = 0.25 * N_{Exc}$  inhibitory spiking neurons with conductance-based currents introduced in this section. Each excitatory neuron in the population is randomly connected to  $k_{EE} = \frac{N_{Exc}}{100} = 200$  excitatory and  $k_{EI} = \frac{k_{EE}}{4}$  inhibitory neurons and each inhibitory neuron is connected to  $k_{IE} = k_{EE}$  and  $k_{II} = \frac{k_{EE}}{4}$  excitatory and inhibitory neurons, respectively. The weights of excitatory synaptic connections are in a range that 10 – 20 synchronous excitatory spikes suffice to depolarize the target neuron to the level of its firing threshold when it is initially at rest at the time of input arrival. Weights are being drawn from a log-normal probability density with low variance. Therefore, approximately  $O(\sqrt{k_{EE}})$  spikes are adequate

for firing. Assuming homogeneity in the population as we have discussed in the introduction we can build a mean-field equation for the excitatory and inhibitory population in this sparse network, assuming each neuron receives input with the same statistics.

## 3 Results

### 3.1 Response of a single neuron to the Poisson input

In this section, we want to consider the response of the neuron to a specific type of current, namely Poisson input. The reason to consider this type of input is that in an asynchronous firing state neurons receive Poisson input from other neurons. Assume that the number of afferents to each neuron is high and the population activity is nearly constant with firing rate  $r$ . Assuming homogeneity in the number of connections and weights, then at any moment the probability distribution that for a neuron,  $k$  presynaptic neurons out of a total number of  $n$  presynaptic neurons are active is a binomial  $f(n, k, R) = \binom{n}{k} R^k (1 - R)^{n-k}$  which in the regime  $R \ll 1$  is well approximated by a Poisson distribution with parameter  $nR$ .

We first study the response of the neuron to a non-fluctuating constant periodic synaptic current. Suppose the target neuron receives constant numbers  $\rho_E$  and  $\rho_I$  of excitatory and inhibitory spikes per unit time, with all the excitatory spikes having the same strength  $w_E$  and all the inhibitory spikes having the strength  $w_I$ . The conductance of the excitatory channels  $g_{exc}(t)$  is modified by excitatory spikes arriving at times  $s < t$ :

$$g_{exc}(t) = \int_{-\infty}^t g_{exc}^0 w_E \rho_E \exp\left(-\frac{t-s}{\tau_{syn}^{exc}}\right) ds = g_{exc}^0 w_E \rho_E \tau_{syn}^{exc} \quad (5)$$

The same formula applies for the constant inhibitory current. The potential of the target neuron fed by this current will reach a stationary value. If this stationary limit is greater than  $V_{th}$  then the target neuron will fire periodically. This constraint reads as:

$$\rho_I < \frac{g_{leak} * (V_{th} - V_{rest}) + g_{exc}^0 * w_E * \rho_E * \tau * V_{th}}{g_{inh}^0 * w_I * \tau * (V_{inh} - V_{th})} \quad (6)$$

The stationary limit of the potential is a weighted average of reverse potentials,

$$V_{st} = \frac{g_L V_L + g_{exc}^0 w_E \rho_E \tau V_{Rexc} + g_{inh}^0 w_I \rho_I \tau V_{Rinh}}{g_L + g_{exc}^0 w_E \rho_E \tau + g_{inh}^0 w_I \rho_I \tau} \quad (7)$$



If input rates satisfy Equation 6, the output firing rate will be

$$\rho_{out} = (g_{leak} + g_{exc}^0 w_E \rho_{E\tau} + g_{inh}^0 w_I \rho_{I\tau}) * \left( \log \frac{V_{rest} - V_{st}}{V_{th} - V_{st}} \right)^{-1} \quad (8)$$

The left-dashed curves in Figure 1 show the output firing rate for three different values of excitatory input rate versus inhibitory input rate. In the rest of this section we take the input to the neuron as stationary homogeneous Poissonian inhibitory and excitatory spike trains. In this case the number of spikes in a time interval  $\Delta t$  follows a Poisson distribution:

$$p(k_{[t, t+\Delta T]}) = (\lambda \Delta T)^k \frac{e^{-\lambda \Delta T}}{k!} \quad (9)$$

The output firing rate of the neuron to the Poisson input is depicted in Figure 1A. Compared to the constant input with the same constant rate as the Poisson rate  $\lambda$ , the curve becomes smoother and the transition from silent state to active state does not show a sharp jump. Below the critical inhibition value, the neuron output follows the mean-field deterministic trajectory, however close to this point the fluctuation effect caused by stochastic arrival of spikes manifests itself. Moreover, the stochasticity in the input leads to stochastic firing at the output. Figure 1B shows how the coefficient of variation of the firing time interval of the output spike train change according to the input. This quantity is calculated as

$$CV(\delta t) = \frac{\sigma_{\delta t}}{\langle \delta t \rangle} \quad (10)$$

where  $\delta t$  is the set of firing time intervals of the response of the target neuron subjected to a stationary Poisson input. When the excitatory input is much stronger than the inhibitory one the output firing pattern becomes more regular and the CV value is small. However, close to the inhibition cutoff, CV becomes close to unity, which is characteristic of the Poisson point process.

The Poisson input in the limit of a high firing rate and small synaptic weights can be approximated by a diffusion process. Suppose, in the time interval  $[t, t + dt]$ ,  $N(t, t + dt)$  excitatory spikes arrive at the cell each with synaptic strength  $w_e$ . As the spike arrival is a Poisson process with the rate  $\lambda$  the distribution of  $N(t, t + dt)$  is Poisson and all the cumulants of the random variable  $N$  are equal to  $\lambda dt$ . This leads to the following cumulant for  $I(t, t + dt) = w_e N(t, t + dt)$ :

$$\begin{aligned} \kappa_1 &= \langle I_{t, t+dt} \rangle dt = w_e \lambda dt \\ \kappa_2 &= \text{Var}(I_{t, t+dt}) = w_e^2 \lambda dt \\ \kappa_3 &= w_e^3 \lambda dt \end{aligned} \quad (11)$$

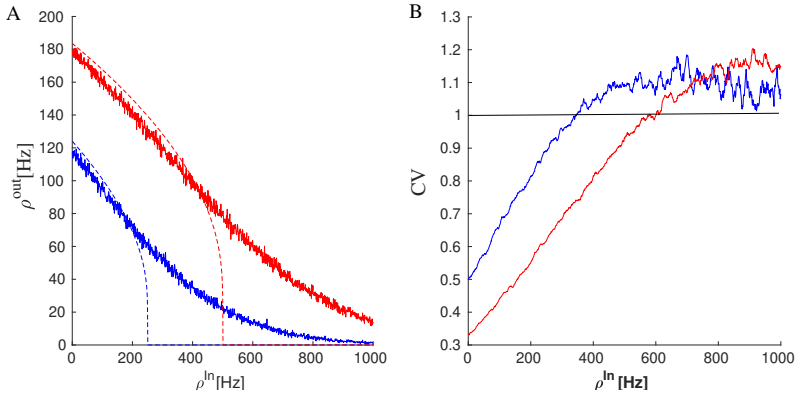


**Fig. 1:** (A) Firing rates of a neuron receiving excitatory Poisson input with two different excitatory rates (the red curve corresponding to the higher one) vs. the Poisson inhibitory input. Dashed lines are the response of the neuron to the constant input with a magnitude equal to the Poisson rates (Equation 8). (B) Coefficient of variation of the spike intervals of a neuron receiving Poisson inputs of the same rates as in the left graph. Near cutoff, the neuron fires with CV close to one.

Higher cumulants can be ignored if we assume that  $w_e^3 \lambda$  goes to zero in the limit of a high number of afferent inputs. In theory, this can be achieved by assuming weights to scale as  $w_e = \frac{W}{\sqrt{k}}$  where  $k$  is the number of presynaptic neurons. In this case,  $\lambda \sim O(k)$  and the average excitatory and inhibitory currents are each of order  $O(\sqrt{k})$ , the variance of the current is of  $O(1)$  and higher cumulants vanish in the limit of large  $k$ . In this case, one can take  $I(t, t + dt)$  as a Gaussian random variable with mean and variance given by the above equation. It can also be written as

$$I(t)dt = w_e \lambda dt + w_e \sqrt{\lambda} dW_t \quad (12)$$

where  $W_t$  is a Wiener process.

In the conductance based model the input to the cell causes a change in the conductance. As the input is stochastic the conductance is also a stochastic variable which can be written as

$$g(t) = \int_{-\infty}^t g_0 e^{-\frac{t-s}{\tau}} I(s) ds = \int_{-\infty}^t e^{-\frac{t-s}{\tau}} g_0 w_e \lambda ds + \int_{-\infty}^t e^{-\frac{t-s}{\tau}} g_0 w_e \sqrt{\lambda} dW_s \quad (13)$$

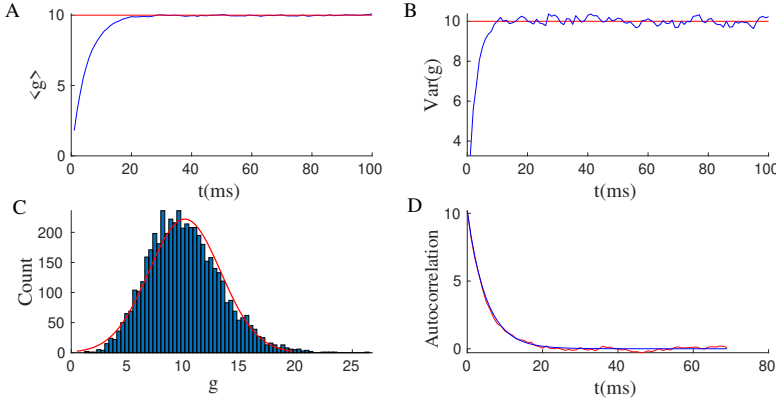


**Fig. 2:** Mean (A), Variance (B), stationary probability distribution (C), and auto-correlation (D) of the conductance  $g(t)$  of a neuron receiving Poisson input. The red lines are the values calculated by the diffusion approximation and the red curve in the bottom left plot is the Gaussian distribution with the mean and variance as derived in the text. The auto-correlation matches Equation 16. This figure shows that the diffusion approximation is valid.

The second term is the integral of a Wiener process with exponential kernel. For a stochastic process  $Y_t = \int_{-\infty}^t f(s) dW_s$ , we can easily verify that:

$$\begin{aligned} \langle Y_t \rangle &= 0 \\ \langle Y_t^2 \rangle &= \int_{-\infty}^t f(s)^2 ds \end{aligned} \quad (14)$$

If we consider a stationary and homogeneous Poisson process as the input then  $g(t)$  will also attain a stationary probability distribution. Using the above equation, mean and variance of  $g(t)$  reach the limits

$$\begin{aligned} \langle g \rangle &= \tau g_0 w_e \lambda \\ \text{Var}(g) &= \frac{\tau g_0^2 w_e^2 \lambda}{2} \end{aligned} \quad (15)$$

With the above scaling of the weights, higher cumulants vanish and one can assume that  $g(t)$  reaches a stationary Gaussian probability distribution with mean and variance as above. The covariance of this process can be derived by direct multiplication and averaging over the noise terms of  $g(t)$  and  $g(t')$  from Equation 15 to reach the following equation when  $t' > t$ :

$$\langle g(t)g(t') \rangle - \langle g(t) \rangle \langle g(t') \rangle = \text{Var}(g) e^{-\frac{(t' - t)}{\tau}} \quad (16)$$

The same procedure applies to inhibitory currents. Figure 2 shows statistics of conductance  $g(t)$  and the validity of diffusion approximation. If we assume that the synaptic time scale  $\tau$  is very small in comparison to the membrane potential time scale, then one can ignore the cross correlation and consider  $Y_t = g(t) - \langle g \rangle$  as Gaussian white noise. In this limit,

$$\lim_{\tau \rightarrow 0} \langle Y_t Y_s \rangle = 2\tau \text{var}(g) \lim_{\tau \rightarrow 0} \frac{e^{-\frac{(s-t)}{\tau}}}{2\tau} = 2\tau \text{var}(g) \delta(t-s) \quad (17)$$

This leads to a stochastic differential equation for the membrane potential evolution in the conductance-based model, when  $v(t) < V_{th}$ :

$$\begin{aligned} C \frac{dv(t)}{dt} = & [g_{Leak}(v_{Leak} - v(t))g_0 w_e \lambda_e \tau (v_{Rexc} - v(t))g_0 w_i \lambda_i \tau (v_{Rinh} - v(t))] \\ & + \xi_{exc}(t)(v_{Rexc} - v(t)) + \xi_{inh}(t)(v(t) - v_{Rinh}) \\ \equiv & [a - bv] + \xi_{exc}(t)(v_{Rexc} - v(t)) + \xi_{inh}(t)(v(t) - v_{Rinh}) \end{aligned} \quad (18)$$

Here  $\xi_{exc}(t)$  and  $\xi_{inh}(t)$  are purely random Gaussian processes:

$$\begin{aligned} \langle \xi_{exc}(t) \rangle &= \langle \xi_{inh}(t) \rangle = 0 \\ \langle \xi_{exc}(t) \xi_{exc}(t') \rangle &= \tau^2 g_0^2 w_e^2 \lambda_e \delta(t-t') \equiv D_e \delta(t-t') \\ \langle \xi_{inh}(t) \xi_{inh}(t') \rangle &= \tau^2 g_0^2 w_i^2 \lambda_i \delta(t-t') \equiv D_i \delta(t-t'). \end{aligned}$$

The first line of Equation 18 is the deterministic evolution of the potential. When the fixed point of the deterministic term,  $v_{det}^{inf} = V_{st} = \frac{a}{b}$  as defined by Equation 18 is greater than  $V_{th}$ , the effect of fluctuations is marginal and the firing of the neuron is governed by the drift term. However, when  $V_{st}$  is below the threshold, fluctuations in the input can result in firing of the neuron. In Appendix .1, we calculate the variance and the mean of the membrane potential and the output firing rate of the neuron in the Gaussian approximation. We can improve the approximation for the potential distribution and the firing rate by considering the autocorrelation in the conductance. When  $\tau$  is not negligible but small, we can use the  $\tau$  expansion method to account for first-order corrections to the Fokker-Planck equation (Appendix .2). Figure 3C shows that these corrections lead to a better approximation of the stationary membrane potential variance in a low firing rate regime. The stationary variance of the membrane potential decreases at higher values of  $\tau_{syn}$  (Figures 3A and 3B). Higher rates in excitatory and inhibitory input would lead to lower stationary variance and lower rates (Appendix .3).

### 3.1.1 Condition for Poisson output

In the model of conductance based synaptic currents, the output spike train is Poisson in the regime of fluctuation driven spiking when the stationary average

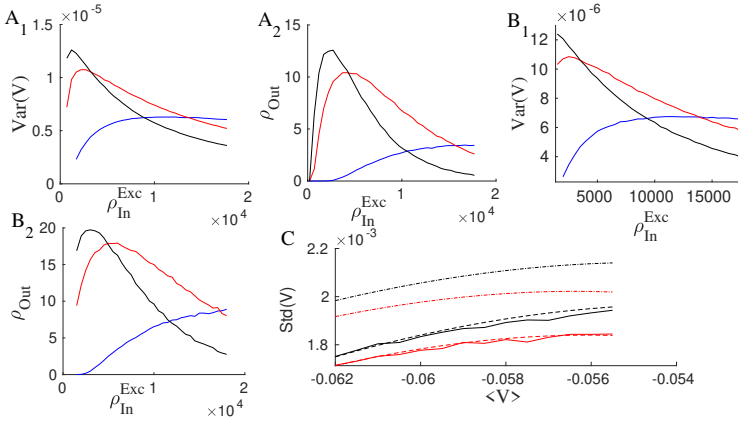


**Fig. 3:** (A1-A2) Stationary variance of the membrane potential and the output firing rates, when the excitatory rate ( $x$ -axis) and inhibitory rates are balanced so that the average membrane potential is at  $-57\text{mv}$  for three different values of  $\tau_{syn} = [1$  (Blue),  $3$  (Red),  $5$  (Black)] ms. (B1-B2) Same with average membrane potential tuned at the threshold value  $-50\text{mv}$ . (C) Stationary potential variance for a neuron receiving two different excitatory input rates,  $1000\text{Hz}$  (red) and  $1600\text{Hz}$  (blue), and corresponding inhibitory input, which places the average potential at a specific value shown in the  $x$ -axis. Solid lines are simulation results, dashed lines correspond to low firing regimes with tau approximation (Equation A2.1), and fine dashed lines show Gaussian approximation. ( $\tau_{syn} = 2.5\text{ms}$ )

potential is away from the threshold. To analyze the condition for Poisson firing, we investigate the case where the stationary membrane potential is below firing threshold. When excitatory and inhibitory currents are matched in a way that the stationary membrane potential  $V_{st}$  is close to the firing threshold  $V_{th}$ , the approximations in the previous section are no longer valid. In the limit of a high number of afferents the drift term would set the average membrane potential to its stationary value in a short time. Here we calculate the mean firing time and variance of it based on the approximation that fluctuations in the input close to the stationary average potential are weakly dependent on the voltage level.

Therefore, our problem is reduced to the well known problem of the first passage time of a Brownian particle evolving as  $\frac{dx}{dt} = -kx + \xi(t)$  to reach the threshold  $a$ .  $\xi$  is white noise with variance  $\sigma$ . We want to approximate results for first passage time moments when the stationary membrane potential is close to the threshold. The goal here is to obtain approximate analytical results for firing rate and CV of the spike time interval to identify conditions for output Poisson firing and linearization of the output rate.

We apply the Siegert formula (Siegert (1951)) for the first passage time (Appendix .4) in our case. Let us take  $x = v - \frac{a}{b}$ ,  $x_0 = v_0 - \frac{a}{b}$  and  $x_{th} = v_{th} - \frac{a}{b}$  where  $\langle V \rangle_{st} = \frac{a}{b}$ . Thus, the random variable  $x$  evolves as  $\frac{dx}{dt} = -bx + \sigma(x)\xi(t)$ . where  $\xi$  is a white noise with unit variance and

$$\begin{aligned} \sigma^2(x) &= \frac{1}{C^2} \{ D_e (v_{Rexc} - \frac{a}{b} + x)^2 + D_i (v_{Rinh} - \frac{a}{b} + x)^2 \} \\ b &= \frac{1}{C} (g_{Leak} + g_0 w_e \lambda_e \tau + g_0 w_i \lambda_i \tau) \end{aligned} \quad (19)$$

For the case of Poisson current to the cell, if the mean value is close to the threshold, the magnitude of fluctuations does not vary much in the interval  $[V_{rest}, V_{th}]$ , therefore in the following we neglect dependence of  $\sigma$  on  $x$ .

The approximation for the mean passage time from the Siegert formula is

$$\begin{aligned} t_1(x_{th} | x_0) &= -\frac{\sqrt{\pi}}{b} \kappa + \left[ \left( \frac{a}{b} - V_{rest} \right) \sqrt{\frac{b}{\sigma^2}} \right] \frac{\sqrt{\pi}}{b} + \frac{\sqrt{\pi}}{b} \left[ (V_{th} - \frac{a}{b}) \right] \sqrt{\frac{b}{\sigma^2}} \\ &\quad + \frac{1}{b} \left[ (V_{th} - \frac{a}{b}) \sqrt{\frac{b}{\sigma^2}} \right]^2 \end{aligned} \quad (20)$$

where  $\kappa$  is very weakly dependent on input rates and we take it as a constant factor (see Eq.A4.4 in Appendix.4). Altogether, we can write down the average rate of firing,  $\rho = \frac{1}{t_1(x_{th} | x_0)}$ , in the case that the average stationary potential is close to threshold as

$$\rho = \frac{b}{\sqrt{\pi}} \left( \frac{1}{\kappa + (V_{th} - \frac{a}{b}) \sqrt{\frac{b}{\sigma^2}}} \right) \quad (21)$$

In Figure 4, we have plotted this rate approximation which causes only a very small error when the average potential is near threshold. If  $\langle v \rangle = \frac{a}{b}$  is constant for balanced inhibitory and excitatory input rates, then the output rate of the neuron would be linearly proportional to the input rates via the factor  $b$ . Moreover the output rate would decrease as  $\frac{1}{x_{th}}$  with the increase of the distance of the stationary average potential from the threshold.

Next, we want to investigate the variance of first passage time. From the recursion formula (Eq.A4.1 in Appendix.4) and after proper approximations we end up with the following expression for the CV of the time interval between

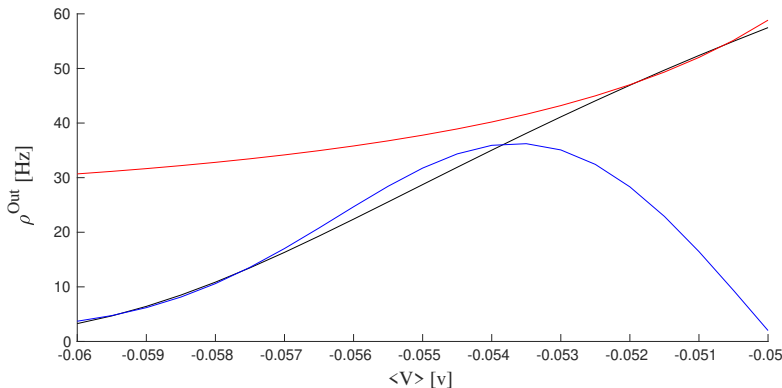


**Fig. 4:** Firing rate approximation by Gaussian assumption of Eq.A1.4 in Appendix.1 (blue) and by near-threshold high firing assumption (red) of Eq.21 are compared with simulation results (black curve). Here, we fix the inhibitory input and select a value of the excitatory input rate that leads to a specific mean stationary membrane potential shown on the  $x$ -axis.

spikes:

$$CV^2 = \frac{Var(t)}{\langle t \rangle^2} \approx 1 + \frac{C}{t_1(x_{th} | x_0)^2} + 2\sqrt{\pi} \ln(2) \frac{\frac{x_{th}}{b\sqrt{b}\sigma}}{t_1(x_{th} | x_0)^2} \quad (22)$$

where  $C$  is a negative constant (see Eq.A4.5 in Appendix.4). The second term is negative and monotonically goes to zero as  $x_{th}$  increases. In the limit of large  $x_{th}$ , the second and the third term both go to zero and  $CV$  approaches 1. However, in the near threshold approximation the maximum of the third term occurs where  $CV$  is approaching 1. Expanding in powers of  $x_{th}$ , we arrive at

$$x_{th}^{opt} := V_{th} - \langle V \rangle_{st} = \frac{\pi\sigma}{2\sqrt{b}} \quad (23)$$

As shown in Appendix.3 (Eq.A3.1),  $\frac{\sigma}{\sqrt{b}}$  reaches a constant value for high input rates. This can be used to determine the value of  $\langle V \rangle_{st}$  that leads to maximal CV. Figure 5 shows the CV of the interspike interval for different sets of excitatory and inhibitory pairs of input. As can be seen, at the threshold, neuronal firing time intervals have lower variance, but the CV approaches one far away from the threshold. The stationary membrane potential value corresponding to the maximal value of CV from Equation 23 is shown in the right diagram and it matches well with the actual values from the simulation. At  $V_P := \langle V \rangle_{st}^{opt} \approx -0.56mv$ , the CV for different input rates has a maximum independently of the rate values.

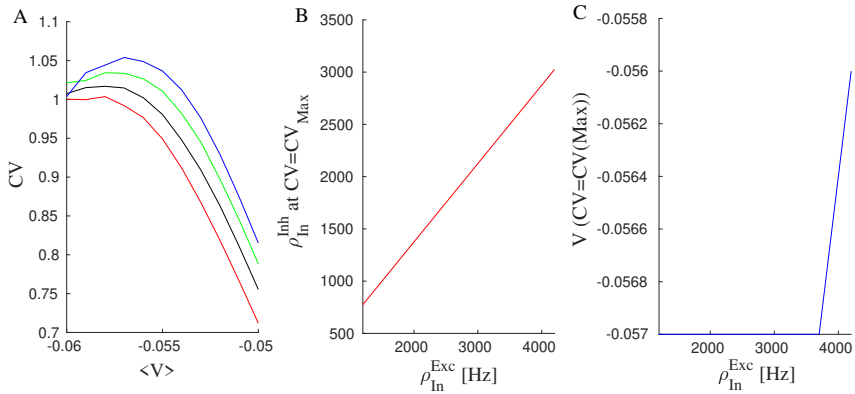


**Fig. 5:** (A) CV of interspike intervals for four different excitatory input rates and their corresponding inhibitory rates, which set the average membrane potential at each specified value shown in the x-axis. (Red curve corresponds to the highest excitatory rate (4000Hz) and the blue one to the lowest rate (1000Hz) ) (B) Inhibitory rate vs. excitatory rate at the maximal  $CV$ . (C) Membrane potential value at the value of the maximal  $CV$ .

In the middle plot, we see that the inhibitory rate which satisfies  $CV = CV_{max}$  varies linearly with the excitatory rates. As can be seen, when the stationary membrane potential is approximately below  $V_P$ , the CV of interspike intervals approaches 1, independently of the values of inhibitory and excitatory rates. This is an indicator that output firing in response to Poisson input is itself a Poisson point process when  $\langle V \rangle_{st}$  lies below  $V_P$ . For a more conclusive result, one has to calculate higher moments or investigate the limit of the FPT probability density when  $x_{th}$  is very large. The fact that the Poisson output condition for different sets of Poisson input leads to approximately a similar level of the membrane potential enables us to introduce the linearization of the output rate at the line corresponding to  $\langle V_m \rangle = V_P$ .

### 3.1.2 Linear Poisson neuron approximation

Here we want to show that linearizing the response curve of a neuron receiving Poisson current near  $V_P$ , introduced in the last subsection, leads to a good approximation for the firing rate of the neuron in a wide range of input rates. The linearization is around the line characterized by Equation 7 with  $V_{st} = V_P$  in the  $\rho_{exc} - \rho_{inh}$  plane. This line corresponds to the balance of mean excitation and inhibition at  $V_P$ . On this balance line from Equation 21, the output rate will depend linearly on the excitatory or inhibitory input rate (see Figure 6).

We want to linearize the output rate around  $V_P$ . For this purpose let us write the equation of the plane passing through the line of current balance at  $V_P$  (Eq.24) and the tangent line in the  $(\rho_E, \rho_{out})$  plane at some arbitrary point  $(\rho_I^0, \rho_E^0, \rho_{out}^0)$ . The balance condition line for an excitatory neuron connected



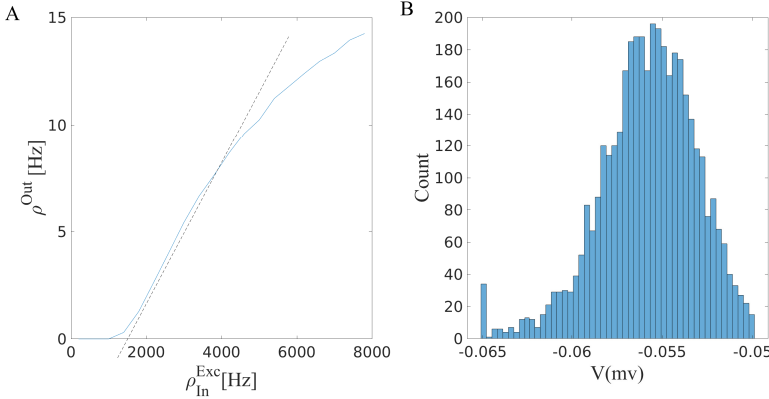


**Fig. 6:** Response of a population of neurons receiving excitatory and inhibitory inputs balanced in a way that the drift term has a fixed point at  $V_P = -0.56\text{mv}$ . (A) Output firing rate for different values of balanced inhibitory and excitatory input rates. The output rate changes semi-linearly on this line and firing in this regime that is driven by the fluctuation in the input causes the neuron to fire with Poisson point process statistics. (B) The stationary potential distribution of the population of neurons. There is a reservoir of neurons close to the threshold while the average firing rate is about 20 Hz. Parameters used:  $w_E = 0.5$ ,  $w_I = 0.75$ ,  $N_E = 7000$ ,  $N_I = 0.25 * N_E$

to  $k_{EE}$  excitatory neurons and  $k_{IE}$  inhibitory neurons each firing with the rate  $\rho_E$  and  $\rho_I$ , respectively, and receiving external excitatory rate  $\rho_{Ext}$  is of the form:

$$\rho_E^e * k_{EE} = \frac{(V_{Rinh} - V_P) * g_{inh}^0 * w_{EI}}{g_{exc}^0 * w_{EE} * (V_P - V_{Rexc})} \rho_I * k_{EI} + \frac{g_{leak}(V_{rest} - V_P)}{\tau * g_{exc}^0 * w_{EE} * (V_P - V_{Rexc})} - \frac{\rho_{Ext}^e}{w_{EE}} \quad (24)$$

We rewrite this in simpler form as  $\rho_E^e = k\rho_I + C$ . The equations for the balance line and the other tangent line in the  $(\rho_E, \rho_{out})$  plane are

$$\frac{(\rho_E - \rho_E^0)}{k} = \rho_I - \rho_I^0 = \frac{\rho_{out} - \rho_{out}^0}{\alpha_{OI}} \quad (25)$$

$$\frac{\rho_O - \rho_O^0}{\beta_{OE}} = \rho_E - \rho_E^0$$

Therefore, the equation of the plane passing through these lines is of the form

$$(\rho_{out} - \rho_{out}^0) = \beta_{OE}(\rho_E - \rho_E^0) + (\alpha_{OI} - \beta_{OE}k)(\rho_I - \rho_I^0) \quad (26)$$

$\beta_{OE}$  is the derivative of the nonlinear response at the selected point in the direction of  $\rho_E$ , and  $\alpha_{OI}$  is proportional to the change of output rate by changing inhibition and accordingly excitation on the balance line. These derivatives do not vary much on the balance line, therefore, the choice of the linearization point does not matter for us at this stage. This suggests that the plane of Equation 26 is tangent to the  $\rho_{out}$  surface. This linear approximation, however, fails for very high excitatory input where the saturation of the neuron causes non-linearity. The linearization point is where the output firing curve has the lowest curvature, and therefore the second derivative vanishes, which makes the approximation error minimal. Figure 7 shows the output firing rate of the target neuron and the linear approximation presented above.

In the next section, we want to investigate the homogeneous firing state of a network. For this purpose we will look at self consistency solutions  $\rho_{out} = \rho_E(in) = \rho_E^*$  for an arbitrary value of inhibitory current. From Equation 26 :

$$(1 - \beta_{OE})\rho_E^* = (\alpha_{OI} - \beta_{OE}k)(\rho_I - \rho_I^0) + \rho_O^0 - \beta_{OE}\rho_E^0 \quad (27)$$

Putting in  $k\rho_I^0 - \rho_E^0 = -C$  and dividing the above equation by  $\beta_{OE}$ , we arrive at

$$\left(\frac{1}{\beta_{OE}} - 1\right)\rho_E^* = -k\rho_I - C + \frac{\alpha_{OI}}{\beta_{OE}}(\rho_I - \rho_I^0) + \frac{1}{\beta_{OE}}\rho_O^0 \quad (28)$$

$\beta_{OE}$  depends on the number of excitatory input to the cell,  $K_{EE}$ , and is related to the proportional change of output firing at the balance line to the change in the firing rate in each excitatory neuron. On the other hand,  $\alpha_{OI}$ , proportional to change in the firing rate while fixing the balance condition, is much smaller than  $\beta_{OE}$ . Therefore, when  $K_{EE}$  is large, the self-consistency equation matches the balance line of Equation 24 with a minimal error.

### 3.2 Sparse homogeneous EI population dynamics

As we have seen for sets of Poisson input that produce low firing output the statistics of spiking events resembles a Poisson process. In a population of neurons there might be a stable stationary or oscillatory population rate with Poisson firing of individual neurons. In this case, the magnitude of fluctuations in the population average scales as  $O(N)$ . This inhomogeneous synchronous or asynchronous firing state exists only in the low firing regime. In the high firing state, the large imbalance of excitatory and inhibitory input leads to periodic firing of the individual neurons which can be also synchronized with high amplitude and high frequency oscillatory population rates. We can use

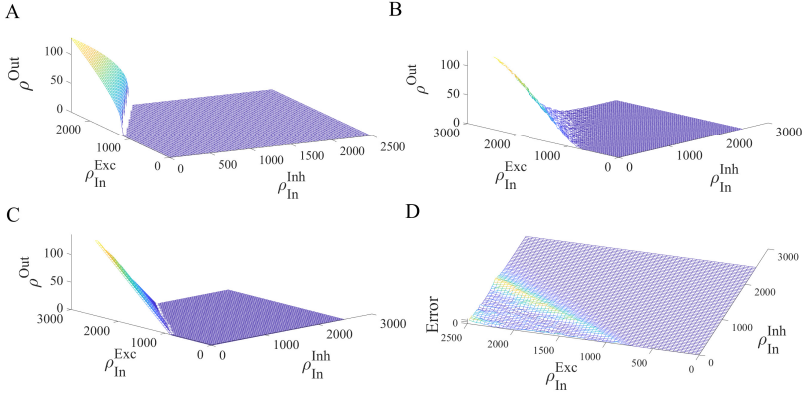


**Fig. 7:** (A) Firing rate of a neuron w.r.t. different values of constant inhibitory and excitatory input. (B) The same for Poisson input. (C) The linear approximation for the output on the critical line of Eq.24. (D) The error of the linear Poisson neuron approximation.

the linear Poisson approximation for identifying and analyzing the dynamics in the low firing rate regime which is of most interest to us. In a homogeneous population, solutions of the self-consistency equations for both inhibitory and excitatory neurons' average output firing rate receiving synaptic currents originated from both neurons in the population and external inhibitory and excitatory currents  $\lambda$  can be written as follows:

$$\rho_E^{st} = f(k_{EE}\rho_E^{st}, k_{EI}\rho_I^{st}, \lambda_{EE}, \lambda_{EI}) \quad (29)$$

$$\rho_I^{st} = g(k_{EI}\rho_E^{st}, k_{II}\rho_I^{st}, \lambda_{IE}, \lambda_{II}) \quad (30)$$

for  $\rho_E, \rho_I \in [0, \rho_{max}]$ . Functions  $f$  and  $g$  are called excitatory and inhibitory gain functions and  $k_{xy}$  is the number of internal connections between neurons in the population. Solving for these gain functions in the general case is not analytically tractable for the EI population. Dynamics to the stationary rates given by equations 29-30 can be phenomenologically approximated by the following mean field equations:

$$\begin{aligned} \frac{d\rho_E}{dt} &= -\frac{1}{\tau_m}(\rho_E(t) - f(k_{EE}\rho_E(t), k_{EI}\rho_I(t), \lambda_{EE}, \lambda_{EI})) \\ \frac{d\rho_I}{dt} &= -\frac{1}{\tau_m}(\rho_I(t) - g(k_{EI}\rho_E(t), k_{II}\rho_I(t), \lambda_{IE}, \lambda_{II})) \end{aligned} \quad (31)$$

This set of equations may have multiple solutions and changing control parameters can lead to Hopf and saddle-node bifurcations, which in turn produce/destroy oscillations or produce/destroy pairs of fixed points. Although it is possible to numerically investigate the FPE for EI populations and its bifurcation diagram, in the next subsections, we follow another approach by using linearized nullclines approximation and logistic function approximation for functions  $f$  and  $g$ . We show that studying these model systems is appropriate for the bifurcation analysis and agrees with simulation results.

### 3.2.1 Linearized nullclines

Function  $f$  in the Equation 29 for the stationary excitatory rate is of the form of an S-shape or sigmoidal curve. Therefore, this equation has one or three solutions depending on the value of the inhibitory rate. This is shown in Figure 8A for three different total inhibitory currents. For a low to a moderate value of inhibition there exist three fixed points, i.e. intersections of the linear line with the sigmoidal gain function, at quiescent state, semi-linear section, and high firing state. Increasing the inhibitory input rate causes the nonlinear gain function to move to the right to the point specified in the graph by a blue dot, and eventually the middle saddle and high fixed point annihilate each other through a saddle-node bifurcation. On the other hand, increasing external excitatory input will move the graph upward, which leads to the annihilation of the low fixed point and the saddle through another SN bifurcation. Figure 8D shows the solutions to the equation 29 for a typical sigmoidal gain function and different values of total inhibitory current to the excitatory population. This is plotted for two different values of  $w_{EE}$  with the dashed curve corresponding to higher  $w_{EE}$ .

Similarly, Figure 8C is the plot corresponding to the Equation 30. Here, the nonlinear sigmoid function  $g$  is plotted for three different values of excitatory current. There exists a single intersection between the line passing through the origin and these curves, which means Equation 30 has a unique solution for the stationary inhibitory rate at each specific excitatory input. Figure 8F is the plot of the location of these intersections for different values of inhibitory input. As can be seen in Figure 8, there exists a semilinear section in the nullcline graphs corresponding to solutions in the linear Poisson section of gain functions. Based on the linear Poisson approximation of the section 3.1.2, the equations for these lines in both excitatory and inhibitory nullcline graphs are:

$$\begin{aligned} \rho_E^{exc} * k_{EE} &= \frac{(V_{Rinh} - V_P) * g_{inh}^0 * w_{EI}}{g_{exc}^0 * w_{EE} * V_P} \rho_I * k_{EI} \\ &+ \frac{g_{leak}(V_{rest} - V_P)}{\tau * g_{exc}^0 * w_{EE} * V_P} - \frac{\lambda_{EE}}{w_{EE}} \end{aligned} \quad (32)$$

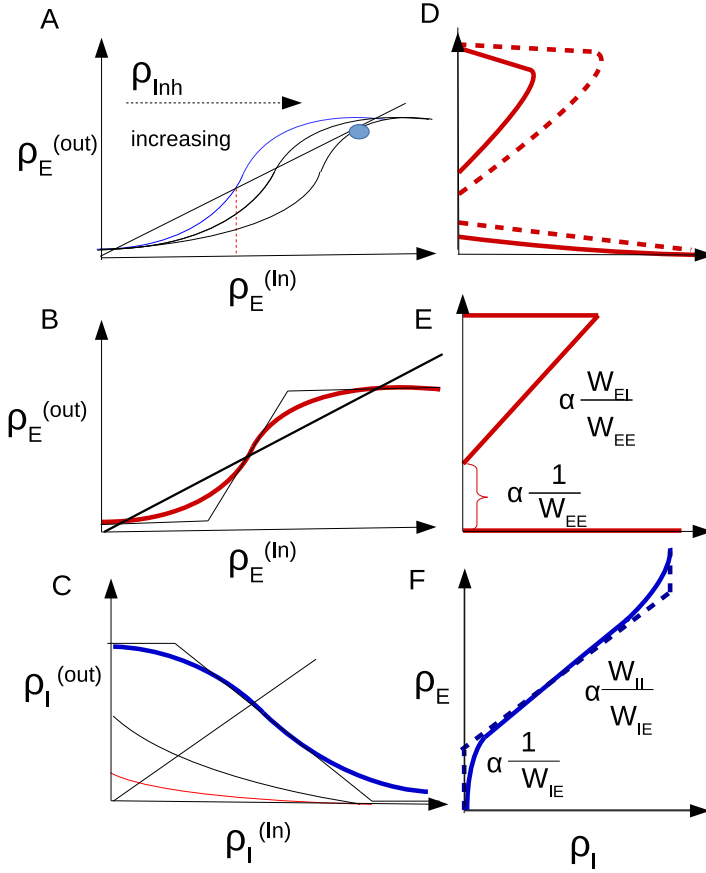


**Fig. 8:** (A) Excitatory neuron output rate vs. excitatory input rate at three fixed values of inhibitory currents. (B) Linearized excitatory gain function. (C) Inhibitory neuron output rate vs. inhibitory input at three different values of excitatory current. (D) Excitatory nullclines of Equations 29-30 for two different values of  $w_{EE}$  with the dotted curve corresponding to the higher value. (E) Linearization of the excitatory nullcline (F) Inhibitory nullcline and its linearization based on Equations 32-33 (dotted curve).

$$\begin{aligned}
 \rho_E^{inh} * k_{IE} = & \frac{(V_{Rinh} - V_P) * g_{inh}^0 * w_{II}}{g_{exc}^0 * w_{IE} * V_P} \rho_I * k_{II} \\
 & + \frac{g_{leak}(V_{rest} - V_P)}{\tau * g_{exc}^0 * w_{IE} * V_P} - \frac{\lambda_{IE}}{w_{IE}}
 \end{aligned} \tag{33}$$

where  $k_{\alpha\beta}$  is the number of excitatory/inhibitory synapse to an excitatory/inhibitory neuron. In the remainder of this work, we assume external inhibitory currents to be zero, in line with our assumption that inhibition is local in our model. We assume  $\frac{k_{EI}}{k_{EE}} = \frac{k_{II}}{k_{IE}}$ , which simplifies our analysis.

In the  $\rho_I - \rho_E$  plane the slope and the  $y$ -intercept of the two lines in Equations 32-33 determine the intersection of the two nonlinear nullclines and can be used to find approximate locations of the bifurcation points of Equation 31. We choose  $\langle w_{EE} \rangle$  and  $\rho_{Ext} = \lambda_{EE}$  as control parameters of our model. Therefore, we first discuss how their change affects the nullclines of Equations 29-30. Increasing  $\rho_{Ext}$  moves the sigmoid graph in Figure 8A upwards causing the low and middle fixed points to move towards each other. For a sufficiently high value of excitatory rate, these fixed points will disappear by a saddle-node bifurcation. In the excitatory nullcline graph (Figure 8D) increasing  $\rho_{Ext}$  shifts the graph to the right. Increasing  $W_{EE}$  will both reduce the  $y$ -intercept of the excitatory nullcline and the slope of the linear section as shown in Fig. 8D. The nullcline for the inhibitory rate equation stays intact under change of control parameters.

The intersections of the inhibitory and excitatory nullclines are solutions of the set of rate equations 29-30. Based on the number of fixed points and their stability, the system can show bi-stability of quiescent and high firing, oscillatory dynamics, avalanches, high synchronized activity, and quiescent state. Investigating the linearized sections of the graphs can help us identify different regimes of activity. The slope and  $y$ -intercept of the linear sections of both nullclines can be compared for this purpose. Based on the Poisson neuron approximation there exists a point in control parameter space where the  $y$ -intercept and slope of two nullclines are equal. This point is the solution of the following linear constraints:

$$s_{exc} := \frac{w_{EI}k_{EI}}{w_{EE}k_{EE}} = \frac{w_{II}k_{II}}{w_{IE}k_{IE}} := s_{inh} \quad (34)$$

$$y_{exc} := \frac{d - \rho_{Ext}}{w_{EE}k_{EE}} = \frac{d - \lambda_{IE}}{w_{IE}k_{IE}} := y_{inh} \quad (35)$$

where  $d$  is a constant equal to  $\frac{g_{leak}(V_{rest} - V_{th})}{\tau * g_{exc}^0 * (V_{th} - V_{Rexc})}$ .

Figure 9A shows the case in which  $w_{EE}w_{II} > w_{EI}w_{IE}$  and the  $y$ -intercept of the excitatory nullcline is lower than the inhibitory one. This occurs in the regime of a low to moderate imbalance of excitatory and inhibitory external input and high excitatory synaptic weight. In this case, the quiescent and the high firing fixed point are both stable and separated by a saddle. Increasing external excitatory input, the excitatory nullcline are shifted to the right and the middle saddle and quiescent node disappear by a saddle-node bifurcation

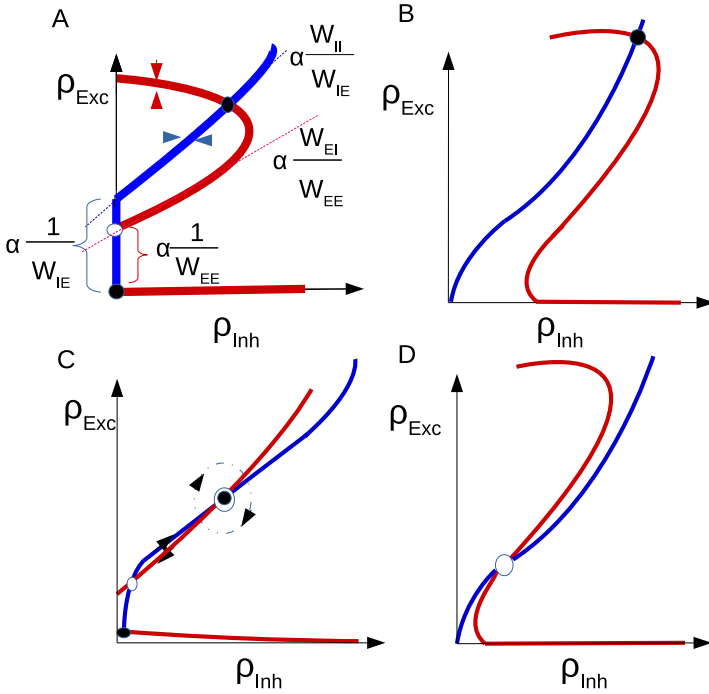


**Fig. 9:** Nullcline diagrams corresponding to regimes of bistability (A), high synchronized firing (B), avalanches (C) and oscillatory dynamics (D). Red curves are excitatory nullclines (Eq.29) and blue curves are inhibitory nullclines (Eq.30).

and only the high firing synchronous state remains (Figure 9B). Increasing  $w_{EE}$  has the same qualitative effect. However, decreasing external input or  $w_{EE}$  drives the system to a quiescent state through different sets of bifurcations depending on the initial state of the system and in general on other parameters of the model. This intermediate transition state involves the appearance of a fixed point in the linear section.

When  $s_{exc} > s_{inh}$  while  $y_{exc} < y_{inh}$ , there is a fixed point in the linear section as depicted in Figure 9C. We will discuss the stability of the fixed point on the linear segment in the following sections. By increasing external input, the quiescent fixed point and the low saddle move closer to each other while the fixed point on the linear section ascends to higher rate values. After the saddle-node bifurcation at the low rate, only the fixed point on the linear section survives as shown in Figure 9D. These two arrangements when the fixed points are close to low firing regimes are important for us because of the avalanche dynamics that appear near this region. The intersection point of the nullclines in the semilinear regime can be approximated by the intersection

point of the linearized nullclines which is:

$$\begin{aligned}\rho_E^c &= \frac{\tau g_0(V_E^R - V_{th})(c_{II}\rho_{Ext} - c_{EI}\lambda_{IE}) + g_L(V_L - V_{th})(c_{II} - c_{EI})}{\tau(c_{IE}c_{EI} - c_{EE}c_{II})} \\ \rho_I^c &= \frac{\tau g_0(V_E^R - V_{th})(c_{EE}\lambda_{IE} - c_{IE}\rho_{Ext}) - g_L(V_L - V_{th})(c_{IE} - c_{EE})}{\tau(c_{IE}c_{EI} - c_{EE}c_{II})}\end{aligned}\quad (36)$$

where  $c_{xy} = k_{xy}w_{xy}g_y(V_y^R - V_{th})$ .

As discussed previously, in the intermediate parameter range, the high fixed point might become unstable through either an Andronov-Hopf or a saddle node bifurcation. Figures 10-11 show nullcline graphs and population activity when the high fixed point loses stability by a Hopf bifurcation. Fig.10A shows nullclines of a system that has stable high and quiescent fixed points with a saddle node at low rates. By decreasing  $w_{EE}$ ,  $s_{exc}$  approaches  $s_{inh}$ , while sufficient external input guarantees that  $y_{exc} < y_{inh}$  during this parameter change. In this particular setup, the inhibitory nullcline is semi-linear and we may speculate that the high fixed point goes through a Hopf bifurcation when the return point of the excitatory nullcline touches the inhibitory nullcline which takes place at some value  $w_{EE}^* \in [0.55, 0.75]$ . Decreasing  $w_{EE}$  further, the high saddle node descends through a linear segment and gets closer to the lower saddle point (Fig.10B). The limit cycle becomes unstable by a saddle separatrix loop bifurcation. After saddle-node annihilation of low and high saddles, the system will end up in the quiescent state for low values of  $w_{EE}$  (Fig.10C). Population activity in these three regimes is shown in Fig.11. Neurons are firing synchronously at a high rates in three different sub-populations in the first case. The high oscillatory activity appears in the second regime where the unstable saddle, which is encircled by a stable limit cycle, lies close to the high activity region. The membrane potential distribution, in this case, has a higher variance, and neurons fire asynchronously.

On the other hand, Fig.12 shows the case in which a high fixed point loses stability through colliding with the saddle that ascends along the linear section. This situation occurs at a lower level of external input, in which decreasing  $w_{EE}$  causes  $y_{exc}$  to pass above  $y_{inh}$  before the slopes become equal. In this case, the high activity fixed point is annihilated by the saddle point.

In addition to oscillatory activity in the middle range of rates, the EI-population can exhibit non-oscillating asynchronous activity which corresponds to a stable fixed point in the linear regime. Fig.13 is the simulation result of the population rates similar to the setup of the Fig.11 with higher  $w_{II}$ , which, as we will see later, makes the fixed point on the linear section stable.

### 3.2.2 Logistic function approximation of gain functions

In this section, we approximate gain functions by logistic functions to analyze bifurcation diagrams and approximate locations of bifurcaion points. For this



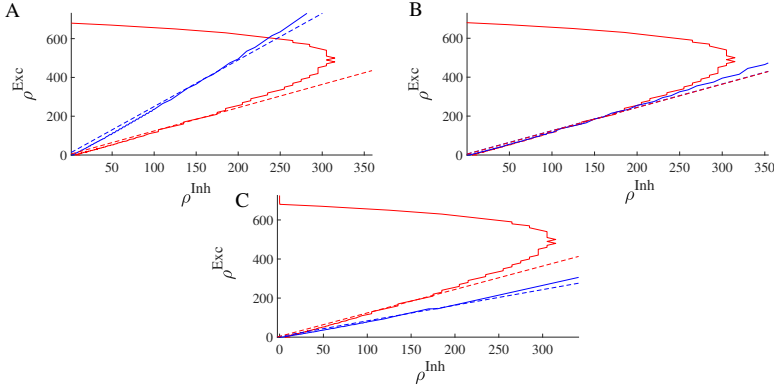


**Fig. 10:** Nullclines for excitatory and inhibitory neuron populations and their corresponding linear approximations of Equations 32-33 obtained from network simulation. Values of parameters are  $w_{EE} = [0.75$  (A),  $0.55$  (B),  $0.4$  (C)],  $w_{EI} = 2$ ,  $w_{II} = 1.5$ ,  $w_{IE} = 0.6$ .

purpose, we consider the gain functions in following form:

$$\begin{aligned}
 g^x(\rho_{Inh}, y_x) &= \frac{\rho_{max}}{1 + \alpha(\rho_{Inh})e^{-ky_x}} - z_0, \\
 y_x &= g_{syn}\tau w_{xI}\rho_{Inh}(V_{Rinh} - V_{th}) + g_{syn}\tau(w_{xE}\rho_{exc} + \rho_{Ext}^x)(V_{Rexc} - V_{th}) \\
 &\quad + g_L(V_{Leak} - V_{th}), \\
 z_0 &= \frac{\rho_{max}}{1 + \alpha(0)e^{-kg_L(V_{Leak} - V_{th})}}
 \end{aligned} \tag{37}$$

Here,  $x$  stands for either excitatory (E) or inhibitory (I) gain functions, which have the same form but different input arguments.  $\rho_{Ext}^x$  is the external excitatory input to the population  $x$ .

At  $y_x = 0$ , balanced input sets the membrane potential at the threshold value and the output rate is approximately  $g_{th} = \frac{\rho_{max}}{1 + \alpha(\rho_{Inh})}$ . Dependence of the output rate on inhibitory input, when the balance condition at threshold holds, is represented by the function  $\alpha$ . At  $y = 0$ , the output rate is proportional to the standard deviation in the input and it can be written as function of the inhibitory input rate as (see Fig.14):

$$g_{th} = b_0 + b_1\sqrt{\rho_{Inh}} \tag{38}$$

which fixes the function  $\alpha(\rho_{Inh})$ .

At equilibrium, the population rates satisfy:

$$\begin{aligned}
 \rho_I &= g^I(\rho_I, c_{IE}\rho_E + c_{II}\rho_I + d\rho_{Ext}^I) - z_0 \\
 \rho_E &= g^E(\rho_I, c_{EE}\rho_E + c_{EI}\rho_I + d\rho_{Ext}^E) - z_0
 \end{aligned} \tag{39}$$

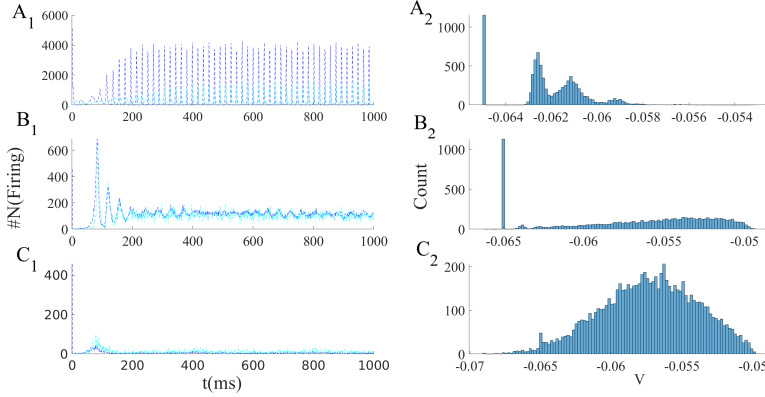


**Fig. 11:** Simulation of populations of  $N_E = 10000$  excitatory and  $N_I = 0.25N_E$  neurons connected by the same average synaptic weight values as in Fig.10. (A1-B1-C1) Number of active excitatory neurons (dark blue) and active inhibitory neurons (light blue) in each time slot of (0.1ms) for three different values of  $w_{EE}$ . (A2-B2-C2) The corresponding stationary membrane potential distribution. In the asynchronous state, the distribution has higher variance.

where  $c_{xy} = ck_{xy}w_{xy}(V_{Ry} - V_{th})$ . As before, we take  $w_{EE}$  and  $\rho_{Ext}^E$  as control parameters. Therefore, the solution of the first equation in Eq.39 is independent of control parameters and gives a curve in the  $\rho_I - \rho_E$  plane. Taking into account that the inverse of  $g(\rho_{Inh}, y)$  is  $g^{-1}(\rho_{Inh}, z) = \frac{1}{k}(\log(\frac{z}{\rho_{max} - z}) + \log(\alpha))$ , the equation for the inhibitory nullcline can be written as :

$$\rho_E = \frac{1}{c_{IE}} \left( \frac{1}{k} \left[ \log\left(\frac{\rho_I + z_0}{\rho_{max} - (\rho_I + z_0)}\right) + \log(\alpha) \right] - c_{II}\rho_I - d\rho_{Ext}^E - g_L \right) \quad (40)$$

The term in brackets accounts for non-linearity in low and high values of  $\rho_I$ . The derivative of this term w.r.t.  $\rho_I$  is  $\frac{\rho_{max}}{\rho_I(\rho_{max} - \rho_I)}$ , which is very small in the middle range of  $\rho_I$  at values close to  $0.5\rho_{max}$ . This is consistent with the fact that nullclines are approximately linear in the middle range of the rates.

To analyze linear stability of the fixed points, we compute derivatives of the gain function:

$$\begin{aligned} \frac{\partial g^x}{\partial \rho_E} &= kc_{xE}g^x \left(1 - \frac{g^x}{\rho_{max}}\right) \\ \frac{\partial g^x}{\partial \rho_I} &= kc_{xI}g^x \left(1 - \frac{g^x}{\rho_{max}}\right) - \frac{1}{\alpha}g^x \left(1 - \frac{g^x}{\rho_{max}}\right) \frac{\partial \alpha}{\partial \rho_I} \end{aligned} \quad (41)$$

Here  $g^x$  stands for  $g^I$  or  $g^E$ . One can substitute  $\rho_I + z_0$  and  $\rho_E + z_0$  from Equation 39 for  $g^I$  and  $g^E$ , respectively. Therefore, the Jacobian matrix

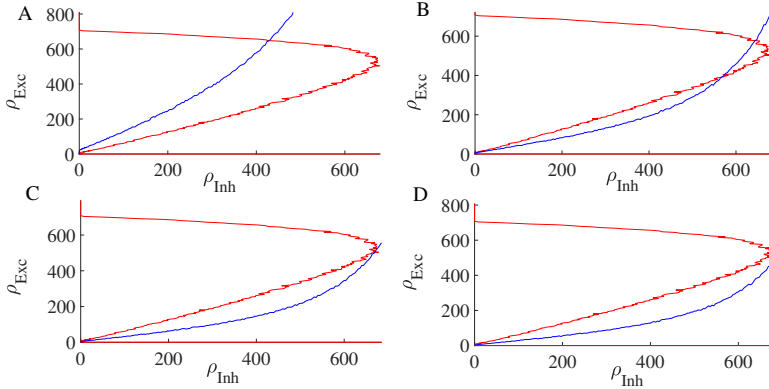


**Fig. 12:** Nullclines for excitatory (red curve) and inhibitory (blue curve) population rates. The parameters used are  $w_{EE} = 0.6$ ,  $w_{EI} = 1.2$ ,  $w_{II} = 0.6$ ,  $w_{IE} = 0.6$  and  $w_{EE} = [0.8(A), 0.6(B), 0.4(C), 0.2(D)]$ . Decreasing  $w_{EE}$  changes the intersections of the two curves.

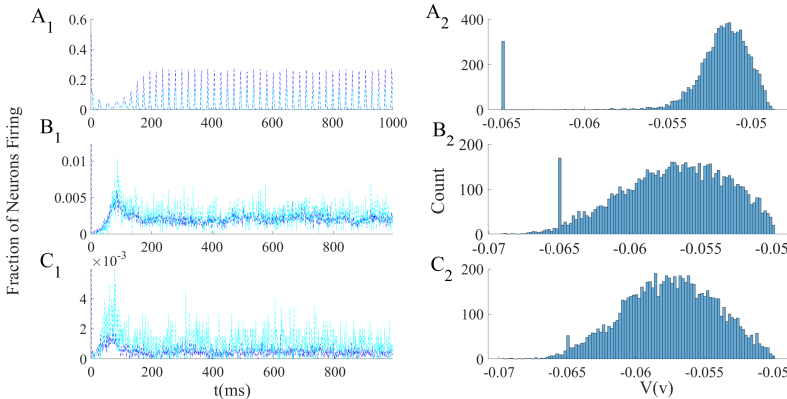


**Fig. 13:** Simulation results of the network with same parameters as in Fig.11 except for  $w_{II} = 2.4$ . The EI population shows asynchronous firing in the medium range of  $w_{EE}$ . This suggest that there is a stable fixed point at the intersection of the linear segments of the excitatory and inhibitory nullclines.

components at the fixed point are:

$$J_{11} = -1 + c_{EE}\rho^E \left(1 - \frac{\rho^E}{\rho_{max}}\right)$$

$$J_{12} = c_{EI}\rho^E \left(1 - \frac{\rho^E}{\rho_{max}}\right) - \frac{1}{\alpha}\rho^E \left(1 - \frac{\rho^E}{\rho_{max}}\right) \frac{\partial \alpha}{\partial \rho^I}$$

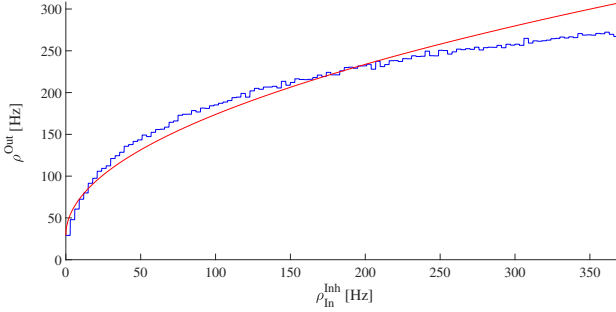


**Fig. 14:** Output rate as a function of input inhibitory rate, when the excitatory rate is selected in a way that average membrane potential of the neuron is  $V_{th}$ . Neuron is operating near a saddle-node bifurcation point at which  $F(I_{syn}) = k\sqrt{I_{syn} - I^*}$ .

$$\begin{aligned}
 J_{21} &= c_{IE}\rho^I\left(1 - \frac{\rho^I}{\rho_{max}}\right) \\
 J_{22} &= -1 + c_{II}\rho^I\left(1 - \frac{\rho^I}{\rho_{max}}\right) - \frac{1}{\alpha}\rho^I\left(1 - \frac{\rho^I}{\rho_{max}}\right)\frac{\partial\alpha}{\partial\rho^I}
 \end{aligned} \quad (42)$$

Hopf bifurcation occurs at fixed point solutions at which the trace of the Jacobian vanishes and its determinant is positive. On the other hand, at saddle-node bifurcation occurs at points where the determinant vanishes. Figure 15 shows the arrangement of excitatory and inhibitory nullclines at Hopf and saddle-node bifurcation points. We proceed to approximate local bifurcation lines in the parameter space.

The condition on zero trace  $Tr(J) = J_{11} + J_{22} = 0$  parameterized by the inhibitory nullcline curve (Eq.40) determines the value for  $w_{EE}$  at which a Hopf bifurcation can occur. Ignoring terms related to  $\alpha$ , which are relatively small, from equating the trace to zero, we have

$$c_{EE}^H = \frac{2 - c_{II} * \rho_I\left(1 - \frac{\rho_I}{\rho_{max}}\right)}{\rho_E\left(1 - \frac{\rho_E}{\rho_{max}}\right)} \quad (43)$$

Then we have  $w_{EE}^H = \frac{c_{EE}^H}{ck_{EE}(V_{RExc} - V_{th})}$ . For each  $(\rho_E, \rho_I)$  point on the inhibitory nullcline (Eq.40), the above equation gives a value of  $w_{EE}$  which sets the trace of the Jacobian to zero at this point. The second equation in Eq.39 which corresponds to the excitatory nullcline determines  $\rho_{Ext}^E$  parameterized by  $\rho_{Inh}$ . Next, we should check the positivity of the determinant to sketch the Hopf bifurcation line in the  $w_{EE} - \rho_{Ext}^E$  plane. Neglecting non-linearities

caused by  $\alpha$ , the determinant of the Jacobian conditioned on zero trace is

$$\det(J)|_{Tr(J)=0} = -\left(1 - c_{II}\rho_I\left(1 - \frac{\rho_I}{\rho_{max}}\right)\right)^2 - c_{IE}c_{EI}\rho_I\left(1 - \frac{\rho_I}{\rho_{max}}\right)\rho_E\left(1 - \frac{\rho_E}{\rho_{max}}\right) \quad (44)$$

At extremely low values of the rates (near zero), the determinant is negative because of the  $-1$  in the above formula. Conditioned on a sufficient amount of inhibitory feedback strength, which is proportional to  $|c_{IE}c_{EI}|$ , the determinant becomes positive at some point and the low fixed point loses stability through a Hopf bifurcation. A point where both determinant and trace of  $J$  are zero, is called a *Bogdanov-Takens* (BT) *bifurcation point*.

Inserting  $\rho_E\left(1 - \frac{\rho_E}{\rho_{max}}\right)$  from  $\det(J)|_{Tr(J)=0} = 0$  into the denominator of the formula for  $w_{EE}^H$  and introducing the parameter  $\gamma = \rho_I\left(1 - \frac{\rho_I}{\rho_{max}}\right)$ , at the BT point in the low rate regime:

$$c_{EE}^{BT} = \frac{\gamma c_{IE}c_{EI}(2 - c_{II} * \gamma)}{(1 - c_{II}\gamma)^2} \quad (45)$$

When  $|c_{II}\gamma|$  is at a moderate value, i.e. sufficiently greater than one :

$$c_{EE}^{BT} \approx \frac{c_{IE}c_{EI}}{c_{II}} \quad (46)$$

If we take number of connections to satisfy  $\frac{k_{EI}}{k_{EE}} = \frac{k_{II}}{k_{IE}}$ , then  $w_{EE}^{BT} = \frac{w_{IE}w_{EI}}{w_{II}}$ . On the semi-linear part of the inhibitory nullcline we have an approximate relation between rates of the form  $\frac{\rho_I}{\rho_E} \approx \frac{w_{IE}}{w_{II}}$ . The determinant on the line of zero trace when  $\rho_E = \frac{w_{II}}{w_{IE}} := \beta\rho_I$  is

$$\det(J)|_{Tr(J)=0} = -1 + 2c_{II}\gamma + (c_{ii}^2 - \beta c_{IE}c_{EI})\gamma^2 \quad (47)$$

The function  $\gamma(\rho_I)$  has a maximum at  $\frac{\rho_{max}}{2}$ . With this in mind, the condition for positive determinant at a potential Hopf bifurcation fixed point at lower rates of the linear regime is

$$\det(J)|_{Tr(J)=0}^L \approx -c_{II}^2\rho_I^2 - c_{IE}c_{EI}\rho_E\rho_I|c_{II}|\rho_I^2(|c_{EI}| - |c_{II}|) > 0 \quad (48)$$

Therefore, if  $|c_{EI}| > |c_{II}|$ , the Hopf bifurcation line survives in the linear regime. On this line,  $w_{EE}^{Hopf} \approx \frac{2 - c_{II}\gamma}{c_{EE}^0\beta\gamma}$ , which has negative derivative  $\frac{-2}{\beta\gamma^2}$ . Thus, Hopf bifurcation in the linear regime occurs at lower values of  $w_{EE}$  compared to  $w_{EE}^{BT}$ . On the other hand,  $\rho_{Ext}^E$  should increase to satisfy the

fixed point condition of equation 39 for the excitatory rate. Altogether, in the  $(w_{EE} - \rho_{Ext}^E)$  plane, the Hopf bifurcation line extends to lower  $w_{EE}$  and higher  $\rho_{Ext}^E$  from the low BT to high BT.

Ascending on the inhibitory nullcline, we reach the nonlinear high branch of the curve, where a linear relation between rates no longer holds and the second derivative of  $\rho_E^*(\rho_I)$  will increase. In addition,  $\gamma(\rho_{inh})$  decreases towards zero. Taking into account these two facts, on the high branch  $\det(J)|_{Tr(J)=0}^L$  decreases and passes through zero at another Bogdanov Takens point at high rate values. If inhibitory feedback is not strong enough, the conditions for Hopf bifurcation are not satisfied.

To sketch the saddle-node bifurcation line we should look at solutions to  $\det(J) = 0$ . Inserting  $\rho_E(\rho_I)$  from Equation 40 into  $\det(J)$ , for each point on the inhibitory nullcline, there exists some  $w_{EE}$  for which  $\det(J) = 0$ . The only condition to check is  $w_{EE} > 0$ . Again the condition that the excitatory nullcline intersects the inhibitory one at the fixed point determines  $\rho_{Ext}$ . Along the semi-linear section of the nullcline, the condition  $\det(J) = 0$  translates into the alignment of the slopes of the linearized nullclines. Therefore, along this section  $w_{EE}$  varies very little.

Figure 15 shows Hopf and saddle-Node bifurcation lines with parameters written in the caption. As can be seen, there exist two Bogdanov -Takens bifurcation points at low and high values of external input corresponding to the intersection of nullclines in low and high firing rate regimes.

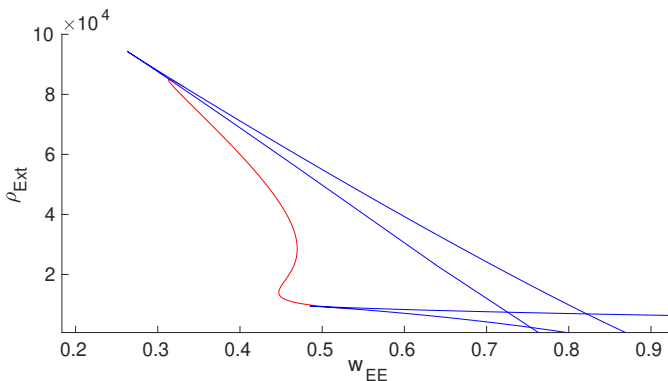


**Fig. 15:** Local bifurcation diagram in the control parameter plane  $(W_{EE}, \rho_{Ext})$ . The red curve is the Hopf bifurcation line and the blue curves are saddle-node bifurcation lines. The free parameters of the model are  $\rho_{Ext}^{Inh} = 300Hz$ ,  $W_{II} = 1$ ,  $W_{EI} = 1.8$  and  $W_{IE} = 0.6$ .

Figure 16 is the bifurcation diagram at low rates. Different regimes of phase space corresponding to different numbers and/or types of fixed points have been labeled. The system has between one and five fixed points. Region (1) with low values of  $W_{EE}$  and external input strength is the quiescent state

with only one stable fixed point. In region (2), there is only an unstable fixed point surrounded by a stable limit cycle corresponding to the intersection of nullclines in the semi-linear sections. In regions (3) and (4) near the BT point, two other fixed points exist at low firing rates. The type of solution in these regions will be discussed later in this section. Region (5) corresponds to the case where there exist 5 intersection points on the nullcline map and the bi-stability of the quiescent and the high state which survives after the annihilation of unstable nodes on the middle section of the nullcline to the region (6). Finally, in the region (7), at high external input and synaptic weight, the only existing fixed point is the high firing one.

Dashed lines are the constraints of Equations 34-35 corresponding to equal slope and  $y$ -intercept of the linearized nullclines. The vertical line is the value of  $w_{EE}^*$  that matches the slopes, for  $w_{EE} < w_{EE}^*$  the inhibitory feedback is getting stronger. The oblique line shows values of  $\rho_{Ext}$  for each  $w_{EE}$  that equalize  $y$ -intercepts of linearized nullclines. In the region below this line  $y_{inh} < y_{exc}$  and vice versa.

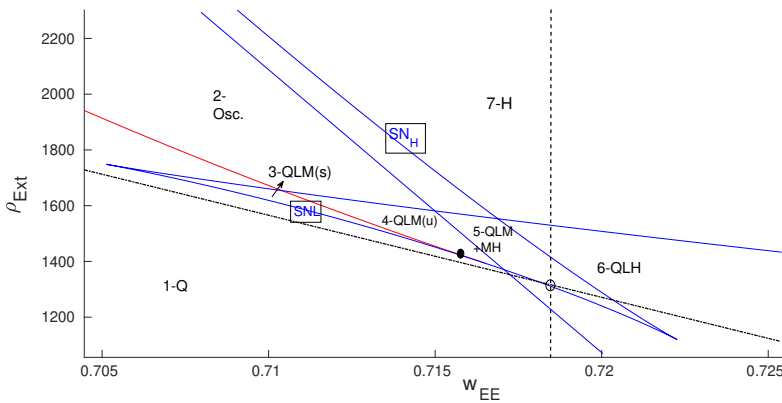


**Fig. 16:** Zoom in on the local bifurcation diagram at low firing rates and the corresponding regimes of phase space with different numbers of fixed points. The dashed line is the condition on the equal slope of linearized nullclines and the semi-dashed line is the condition on equal  $y$ -intercepts. The BT point (black dot) is close to the intersection of these lines. In the labeling of regions (Q) denotes the quiescent state fixed point, (L) is the fixed point at low firing rate, (M) is the fixed point in the linear section, and (H) is the high firing fixed point.

### 3.2.3 Dynamics near the BT bifurcation point

The exact locations of the BT points ( $c_{EE}^{BT}, \rho_{Ext}^{BT}, \rho_E^{BT}, \rho_I^{BT}$ ) are solutions of  $\det(J) = Tr(J) = 0$  and  $g_E(i_E) = g_I(i_I) = 0$ . Figure 17 shows nullcline

arrangements near the low BT point and the global saddle separatrix loop bifurcation line which annihilates the limit cycle solution of the region (3), shown in the same figure. In the previous section, we showed that the low BT

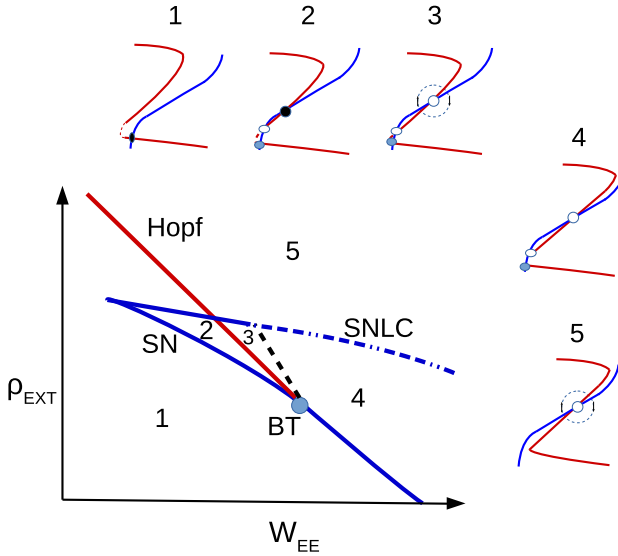


**Fig. 17:** Nullcline arrangements near the BT point. The black dashed line is the saddle-separatrix loop bifurcation and the blue dotted-dashed is the saddle-node on limit cycle (SNLC) bifurcation line.

point is located close to the matching condition for the  $y$ -intercept and the slopes of the linearized nullclines, which we rewrite here:

$$\begin{aligned} c_{EE}^* &= \frac{c_{IE}c_{EI}}{c_{II}} \\ \rho_{Ext}^{E*} &= \frac{c_{EE}^*}{c_{IE}} (\rho_{Ext}^I - d) + d \end{aligned} \quad (49)$$

where  $d$  is a constant defined in Equation 35 .

At the BT point the linearized matrix is of the form:

$$J_{BT} = \begin{pmatrix} \alpha & -\beta \\ \alpha^2 & -\alpha \\ \beta & -\alpha \end{pmatrix} \quad (50)$$

where  $\frac{\beta}{\alpha} = \frac{c_{EI}}{c_{EE}} = \frac{c_{II}}{c_{IE}}$ . At the BT point, the Jacobian has a double zero eigenvalue and with proper coordinate transformation, it can be written in the



form:

$$J = \begin{pmatrix} 0 & 1 \\ 0 & 0 \end{pmatrix}$$

Consider the system in the vicinity of the BT bifurcation point

$$\frac{dz}{dt} = f(z, \mu) = Jz + F(z), z, \mu \in \mathbb{R}^2 \quad (51)$$

Suppose that at  $\mu = 0$ , the system has a fixed point at  $z_0$  with a Jacobian with a zero eigenvalue of multiplicity two. At the BT point, there exist two generalized eigenvectors  $q_0$  and  $q_1$  such that

$$Jq_0 = 0, Jq_1 = q_0$$

Also for  $J^T$  we select vectors  $p_{0,1}$  by

$$J^T p_1 = 0, J^T p_0 = p_1$$

with normalization

$$\begin{aligned} \langle p_0, q_0 \rangle &= \langle p_1, q_1 \rangle = 1 \\ \langle p_0, q_1 \rangle &= \langle p_1, q_0 \rangle = 0 \end{aligned}$$

By linear change of coordinates with transformation matrix  $T = (q_0, q_1)$ , i.e.,  $x = Tz$ , our system can be written as

$$\begin{pmatrix} \dot{x}_1 \\ \dot{x}_2 \end{pmatrix} = \begin{pmatrix} 0 & 1 \\ 0 & 0 \end{pmatrix} \begin{pmatrix} x_1 \\ x_2 \end{pmatrix} + \begin{pmatrix} f(x_1, x_2) \\ g(x_1, x_2) \end{pmatrix} \quad (52)$$

Introducing a direction-preserving time reparametrization and smooth invertible parameter changes, we can transform the system to the normal form:

$$\begin{aligned} \frac{y_1}{d\tau} &= y_2 \\ \frac{y_2}{d\tau} &= \epsilon_1 + \epsilon_2 y_1 + a_2 y_1^2 + b_2 y_1 y_2 + O(y_1 y_2^3) \end{aligned} \quad (53)$$

$\epsilon_{1,2}(\mu)$  are transformed bifurcation parameters,  $a_2 = g_{xx}/2$  and  $b_2 = g_{xy} + f_{xx}$  and  $dt = (1 + \Theta x_1)d\tau$ . The  $y$  coordinates relate to the original  $z = T^{-1}x$  coordinates via :

$$\begin{aligned} u_1 &= x_1, & y_1 &= u_1 \\ u_2 &= \dot{x}_1, & y_2 &= u_2 + \Theta u_1 u_2 \end{aligned} \quad (54)$$

where  $\Theta = g_{yy} + 2f_{xy}$ . Fixed points of the normal form of Equation 53 are  $(y_1, y_2) = (\pm\sqrt{\frac{-\epsilon_1}{a_2}}, 0)$ . Taking  $a_2 > 0$ , when  $\epsilon_1 < 0$ , there exist two fixed points, with Jacobian

$$\begin{pmatrix} 0 & 1 \\ \pm 2\sqrt{\frac{-\epsilon_1}{a_2}} & \epsilon_2 \pm b_2\sqrt{\frac{-\epsilon_1}{a_2}} \end{pmatrix}$$

$y_0^+$  is a saddle in  $\epsilon_1 < 0$  for all  $\epsilon_2$ , while  $y_0^-$  is a sink for  $\epsilon_2 < b_2\sqrt{\frac{-\epsilon_1}{a_2}}$  and a source for  $\epsilon_2 > b_2\sqrt{\frac{-\epsilon_1}{a_2}}$ . When  $b_2 > 0$ , then the line  $\epsilon_2 = b_2\sqrt{\frac{-\epsilon_1}{a_2}}$  is a sub-critical Hopf bifurcation and when  $b_2 < 0$  the same line is a supercritical Hopf bifurcation. To summarize, defining  $\sigma = \text{sgn}(a_2 * b_2)$ , if  $\sigma$  is negative then a stable limit cycle appears and the Hopf bifurcation is supercritical (Fig.18A), but if  $\sigma$  is positive, we have a sub-critical Hopf bifurcation (Fig.18B). As shown in Figure 18, near the BT point apart from local bifurcations, i.e., Hopf and saddle-node, there is saddle-node separatrix loop bifurcation which annihilates the stable or unstable limit cycle that is produced by a super- or sub-critical Hopf bifurcation, respectively.

Linearization near the BT point can help us to identify regimes surrounding it without having to calculate the  $\sigma$  parameter. Nullcline maps related to regions (2) and (3) in Fig.17 shed light on the type of BT bifurcation. In the plot corresponding region (3),  $w_{EE}$  is higher which means that the Jacobian at the fixed point has lower determinant and higher trace. Of the two fixed points in regions (2) and (3) at the semi-linear section the one in the higher  $W_{EE}$  regime is the unstable point. Therefore, in our case near the low BT point the phase space resembles the one in Fig.18B. Increasing  $w_{EE}$  from region (2) will result in loss of stability of the fixed point in the linear branch by Hopf bifurcation, as the trace of the Jacobian at the fixed point becomes zero. However, as we increase the  $w_{EE}$ , slope of the linearized approximation of the nullclines which are tangent to the stable and unstable manifolds of the saddle point that separate the quiescent fixed point and the limit cycle solution, get closer to each other. At some point, these manifolds cross over and therefore destroy the limit cycle solution through a saddle-node separatrix loop bifurcation and we end up with a fixed point of source type at the intersection of nullclines in the linear firing regime of region (4) in Fig.17.

By writing the normal form we can analyze the type of BT from explicit linearization. For the case of  $J_{BT}$  in equation 50, generalized eigenvectors are  $q_0 = (1 \ \alpha/\beta)$ ,  $q_1 = (1 \ (\alpha - 1)/\beta)$ ,  $p_1 = (1, -\beta/\alpha)$  and  $p_0 = (1/\alpha - 1, \beta/\alpha)$ . Therefore, new parameterized coordinates are  $x_1 = E/\beta - \alpha/\beta(E - I)$  and  $x_2 = E - I$ . The normal form parameters  $a_2$  and  $b_2$  are

$$a_2 = \frac{1}{2} \langle p_1, F(q_0, q_0) \rangle$$

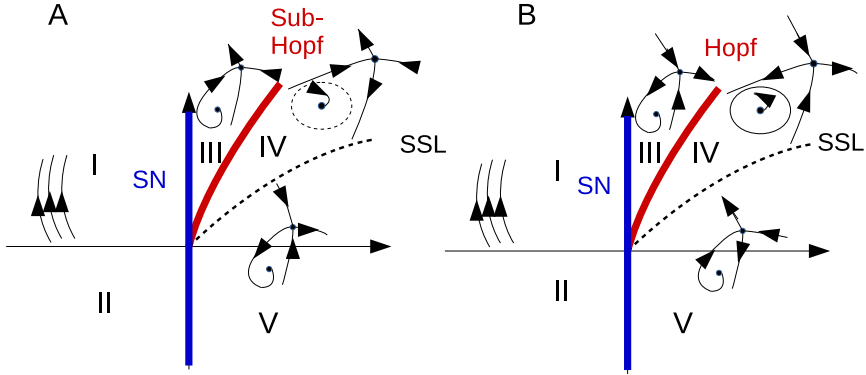


**Fig. 18:** Dynamic flow near the high BT point (A) and the low BT point (B). Blue lines are saddle-node bifurcations, red lines are Hopf bifurcations, and dashed lines are saddle-node separatrix loop bifurcations.

$$b_2 = \langle p_0, F(q_0, q_0) \rangle + \langle p_1, F(q_0, q_1) \rangle \quad (55)$$

where  $F^1(q_0, q_i) = \sum_{l,k} f_{lk} q_0^l q_i^k$  and  $F^2(q_0, q_i) = \sum_{l,k} g_{lk} q_0^l q_i^k$ . Using the logistic gain function, second derivatives in  $E - I$  coordinates can be written as

$$\begin{aligned} g_{EE} &\propto W_{IE}^2 g_I (1 - g_I) (1 - 2g_I) \\ g_{EI} &\propto -|W_{II}| |W_{IE}| g_I (1 - g_I) (1 - 2g_I) \\ f_{EE} &\propto W_{EE}^2 f_E (1 - f_E) (1 - 2f_E) \end{aligned}$$

where  $g_{EI} < 0$ ,  $f_{EE} > 0$  and  $g_{EE} > 0$ . After straightforward but lengthy calculation we can confirm  $\text{sgn}(\sigma) = \text{sgn}(a_2) \text{sgn}(b_2) < 0$  using  $|W_{II}| g_I (1 - g_I) = W_{EE} f_E (1 - f_E)$  and  $\frac{\beta}{\alpha} = \frac{c_{EI}}{c_{EE}} = \frac{c_{II}}{c_{IE}}$  at the lower BT point.

### 3.2.4 Avalanches in the region close to the BT point

We assume that the external input to both excitatory and inhibitory neurons is dominated by the excitatory type and that connections among excitatory populations have a longer range. Therefore, the external excitatory input to the excitatory population is higher than to the inhibitory one. On the other hand, inhibitory connections are local and therefore, follow the dynamics of the adjacent excitatory population. Strong local feedback provided by inhibition prevents the excitatory network to be overloaded. However, it is very closely balanced to set the network near the threshold of activation so that the system can respond efficiently to external input. In the background regime of spontaneous activity, the EI population shows avalanche pattern dynamics and oscillatory behavior. Synchronization of oscillations and the

scale-free avalanche dynamics are characteristic behaviors experimentally validated [Beggs and Plenz \(2003\)](#); [Gong et al \(2003\)](#); [Meisel et al \(2013\)](#). In the sequel, we will see that close to the BT at a low firing rate regime, we can observe both phenomena.

In the parameter space enclosed by Hopf and saddle-node bifurcation lines, i.e., region (4-QLM(u)) in [Fig.16](#), there exist regions with both oscillatory and medium-range Poisson firing states. Decreasing  $W_{EE}$  while changing  $\rho_{Ext}^E$  accordingly, so that the low and medium fixed points move closer to the origin, the system moves towards the Bogdanov-Takens bifurcation point, where the saddle-node bifurcation and Hopf bifurcation lines intersect. In this regime, we see avalanche dynamics in our population. Close to the BT point, the basin of attraction of the quiescent fixed point shrinks and the noise level is high enough for escaping from it. This is in the adjacency of both the saddle-node bifurcation, which creates an unstable low and a weakly stable medium firing fixed point, and the Hopf bifurcation of the quiescent fixed point. This region corresponds to strong inhibitory feedback and sufficient imbalance in external excitatory input. In the nullcline graph, this translates into the state where the  $y$ -intercept of the excitatory graph is lower than the  $y$ -intercept of the inhibitory graph and the slope of the excitatory is larger than the slope of the inhibitory one. Increasing  $W_{EE}$  causes the middle fixed point to move to higher rates and to have a larger basin of attraction. On the other hand, the saddle and the quiescent fixed point move towards each other in the phase diagram and annihilate each other at the saddle-node bifurcation.

[Fig.19](#) shows nullcline arrangements in the region where we observe avalanche patterns. [Fig.19A](#) is the general position of nullclines indicating the fixed point in the linear regime. The other three diagrams correspond to two regimes near the BT point and transition between these two. The diagram in [Fig.19B](#) belongs to the section to the right of BT where there exists a quiescent fixed point with a weakly unstable saddle in the linear section. Here noise causes the system to escape from the basin of attraction of the fixed point which then relaxes in the direction of the nullclines. As nullclines lie on top of each other, the decay time is large and the system shows high synchronous activity while returning to a quiescent state. An increase of external drive or decrease of  $W_{EE}$  leads to saddle-node annihilation which leaves the system with a fixed point at the middle section. [Fig.19C](#) belongs to the state on the left side of BT1 in the vicinity of Hopf bifurcation of the origin. In this case, there is a limit cycle around the saddle point in the linear branch. Like the previous case, adjacency of the fixed point at the origin to the saddle shrinks the basin of attraction of the quiescent state, and therefore noise can bring the system to the limit cycle which itself is sensitive to internal and external noise. Finally, [Fig.19D](#) shows how saddle-nodes of the last two diagrams are annihilated by saddle-node on limit cycle and saddle-node bifurcations, respectively. Here a limit cycle solution emerges. However, close to the origin this limit cycle stays for a longer time in the lower section of very low firing because of slow

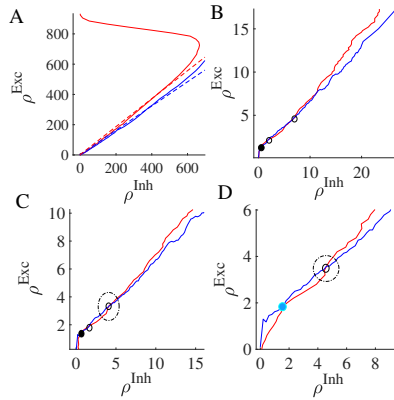


**Fig. 19:** Nullline configuration around the avalanche dynamic region. Red curves are excitatory nulllines and blue curves are inhibitory nulllines.

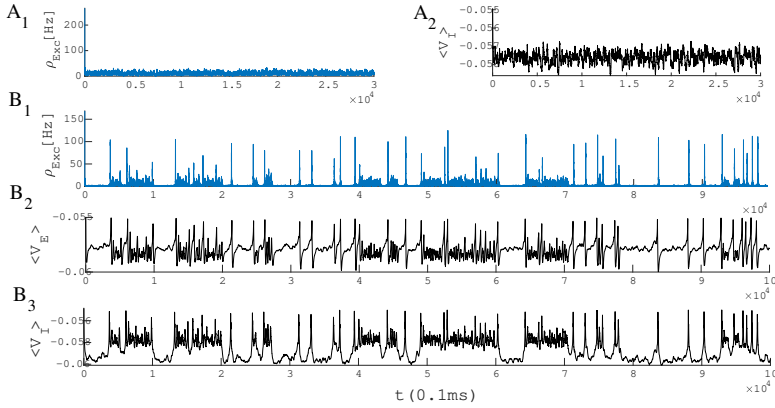
flow in this region. The outcome is again a quasi-periodic burst of avalanches followed by a quiescent state.

Fig.20 shows avalanche characteristics of activity in parameter regime on the left of the BT point with the limit cycle solution very close to the origin (region 3 in Fig.17). Finite size fluctuation leads to switch between these two states. In Fig.20A,  $W_{EE}$  is higher and  $\rho_{Ext}^E$  is slightly lower than the previous case and the system is located in the region with a fixed point in the low firing regime which is stable because of the high value of  $W_{II}$  which corresponds to region (5) in Fig.16. Fig.21B shows avalanche dynamics on the right side of the BT point with an unstable fixed point in the linear section (region (4) in Fig.17). In both sets of figures increasing  $W_{EE}$  moves the system out of the avalanche region with the difference that the fixed point at the linear section is stable in the first case and unstable in the second. Therefore, the nearby regime of activity in the first case (20A) is a non-oscillatory inhomogeneous Poisson firing state while the corresponding regime near the second case is oscillatory (Fig.21A).

### 3.2.5 Stability analysis of fixed points in the linear regime

As we have seen in the last section, close to the BT point there exist regions in which there is a low fixed point at the intersection of the semi-linear sections of nulllines. The stability of the fixed point at the intersection of two nulllines is determined by the Jacobian matrix of the linearized system,

$$A = \begin{pmatrix} -1 + \frac{\partial f}{\partial E} & -\left|\frac{\partial f}{\partial I}\right| \\ \frac{\partial g}{\partial E} & -1 - \left|\frac{\partial g}{\partial I}\right| \end{pmatrix} \quad (56)$$



**Fig. 20:** Avalanches close to the BT point.  $W_{II} = W_{EI} = 2, W_{IE} = 0.75$ ,  $\rho_{Ext}^{inh} = 150Hz$  in both A and B plots. In (A)  $W_{EE} = 0.65$  and  $\rho_{Ext}^{exc} = 218Hz$  and in (B)  $W_{EE} = 0.62$  and  $\rho_{Ext}^{exc} = 223Hz$ . (B<sub>2</sub>) Average membrane potential of excitatory population shows high fluctuation in the avalanches period. (B<sub>3</sub>) Average membrane potential of inhibitory population shows high fluctuation in the avalanches period and two distinct level of polarization. In the quiescent state due to excess external current to the excitatory pool the average membrane potential of the excitatory population is slightly higher than the inhibitory one.

Linear segments intersect if  $y_{inh} < y_{exc}$  and  $s_{exc} > s_{inh}$  or  $y_{inh} > y_{exc}$  and  $s_{exc} < s_{inh}$ . When the slope and  $y$ -intercepts are equal, the Jacobian at the point of intersection is

$$A = \begin{pmatrix} a - \mu & -(b - \frac{b}{a}\mu) \\ a & -b \end{pmatrix} \quad (57)$$

with  $\mu = a \frac{\rho_{Ext}^E - \rho_{Ext}^I}{d - \rho_{Ext}^I}$ .

$$a = \frac{\partial g}{\partial E} = \alpha' W_{IE} K_{IE} = \alpha W_{EE} k_{EE} - 1 + \mu$$

$$d = \frac{g_{leak}(V_{rest} - V_{th})}{\tau * g_{exc}^0 * (V_{th} - V_{Rexc})}$$

$$b = 1 + \left| \frac{\partial g}{\partial I} \right| = 1 + \beta' W_{II} K_{II} = (1 - \frac{\mu}{a})^{-1} [\beta W_{EI} k_{EI}]$$

$$\alpha = g_{exc}^0 \tau_{exc} \frac{(V_{th} - V_{Rexc})}{\sqrt{2\pi\sigma_V^{Exc}}}$$

$$\alpha' = g_{exc}^0 \tau_{exc} \frac{(V_{th} - V_{Rexc})}{\sqrt{2\pi\sigma_V^{Inh}}}$$

$$\beta = g_{inh}^0 \tau_{inh} \frac{(V_{th} - V_{Rinh})}{\sqrt{2\pi\sigma_V^{Exc}}}$$

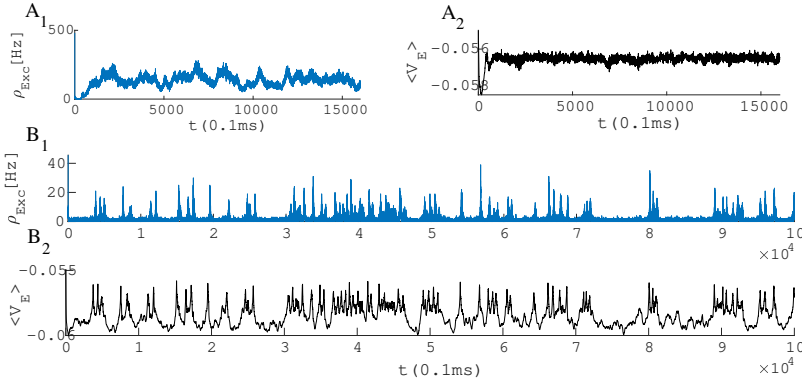


**Fig. 21:** Same as Fig.20 but with new parameters:  $W_{EI} = 1.5, W_{II} = 2, W_{IE} = 0.75$ ,  $\rho_{Ext}^{inh} = 150\text{Hz}$ ,  $\rho_{Ext}^{exc} = 230\text{Hz}$ ,  $W_{EE} = 0.55$  (A1-A2) and  $W_{EE} = 0.52$  (B1-B2).

$$\beta' = g_{inh}^0 \tau_{inh} \frac{(V_{th} - V_{Rinh})}{\sqrt{2\pi\sigma_V^{Inh}}}$$

$$\alpha * \beta' = \beta * \alpha'$$

Because external excitatory input to the excitatory population is greater than to the inhibitory population and inhibitory connections are assumed to be local,  $\mu$  is slightly positive. Define  $E = \rho_E - \rho_E^p$  and  $I = \rho_I - \rho_I^p$ , where  $\rho_I^p$  and  $\rho_E^p$  is the fixed point location at the linear poisson regime with  $\rho_I^p \approx \frac{b}{a}\rho_E^p$ .

At  $\mu = 0$  the eigenvalues of  $A$  are 0 and  $a - b$  with corresponding eigenvectors  $u_1 = (\frac{b}{a}, 1)$  and  $u_2 = (1, 1)$ . By coordinate transformation to  $u_1$  and  $u_2$  coordinates, we can write down the dynamics in the decoupled system as

$$\dot{u} = \begin{pmatrix} 0 & 0 \\ 0 & a - b \end{pmatrix} u \quad (58)$$

where,

$$u = \begin{pmatrix} \frac{b}{a} & 1 \\ 1 & 1 \end{pmatrix}^{-1} \begin{bmatrix} E \\ I \end{bmatrix} = \frac{a}{a-b} \begin{bmatrix} I - E \\ E - \frac{b}{a}I \end{bmatrix} \quad (59)$$

with the transformed initial condition

$$u_0 = \frac{a}{a-b} \begin{bmatrix} I_0 - E_0 \\ E_0 - \frac{b}{a}I_0 \end{bmatrix}$$

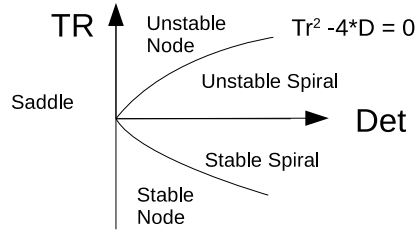


**Fig. 22:** Stability of fixed points in the linear regime based on values of trace and determinant of the Jacobian.

which has the following solution in  $u$  coordinates

$$u(t) = \frac{a}{a-b} \begin{bmatrix} I_0 - E_0 \\ (E_0 - \frac{b}{a}I_0)e^{(a-b)t} \end{bmatrix} \quad (60)$$

Back into  $(E, I)$  coordinates:

$$\begin{bmatrix} E(t) \\ I(t) \end{bmatrix} = \frac{a}{a-b}(I_0 - E_0) \begin{bmatrix} \frac{b}{a} \\ 1 \end{bmatrix} + \frac{a}{a-b}(E_0 - \frac{b}{a}I_0)e^{(a-b)t} \begin{bmatrix} 1 \\ 1 \end{bmatrix} \quad (61)$$

So for this linear system, when  $a - b < 0$ , the initial imbalance of excitatory and inhibitory input leads to a stationary relation of the form  $E = \frac{b}{a}I$ . Now, consider the case in which the linearized nullcline slopes are slightly different with the Jacobian

$$A = \begin{pmatrix} a - \mu & -(b + \epsilon) \\ a & -b \end{pmatrix} \quad (62)$$

Here  $TR = \lambda_1 + \lambda_2 = (a - b) - \mu$  and  $det = \lambda_1\lambda_2 = a\epsilon + \mu b$ . Based on the sign of determinant and trace of the Jacobian at the fixed point, stability is determined (Fig.22). Under the condition that  $b + \mu > a$  and  $\epsilon > -\frac{b}{a}\mu$ , both eigenvalues are negative :  $\lambda_1 = \frac{b\mu - a\epsilon}{b - a}$  and  $\lambda_2 = (a - b) + \frac{2a(\epsilon - \mu)}{a - b}$ . We also have  $|\lambda_1| \ll |\lambda_2|$  for small differences in the slopes. Eigenvectors corresponding to these eigenvalues are

$$\begin{aligned} u_1 &= \left(\frac{b}{a} + \lambda_1, 1\right) \\ u_2 &= (1 + \lambda_2, 1) \end{aligned}$$



Therefore, the dynamics in the linear regime can be projected to the slow stable manifold  $u_1$ . One can approximately write down the evolution of the rates as in Equation 61.

$\epsilon > -\frac{b}{a}\mu$  corresponds to the case that the slope of the excitatory nullcline is higher than of the inhibitory nullcline (stronger inhibitory feedback  $W_{EI}W_{IE} > W_{II}W_{EE}$ ) and the  $y$ -intercept of the excitatory nullcline is slightly lower, i.e. stronger external excitatory input to the excitatory population than to the inhibitory one. Moreover, this is the case when  $W_{II}$  is high enough to guarantee the  $b > a$  condition. When all these requirements are met, the fixed point in the linear segment is stable and we observe an asynchronous low to medium firing state as in Fig.13 and Fig.20. Around this regime, an increase in  $W_{EE}$  will increase  $\mu$  and a change in  $\rho_{Ext}^E$  moves the fixed point along the linear section. The intersection in the linear regime transcends to higher rates by increasing  $W_{EE}$ . This lets the determinant decrease while the trace increases, which eventually destabilizes the fixed point. In the vicinity of the low BT point, based on the value of  $W_{II}$ , in the linear section either a weakly stable or a weakly unstable fixed point surrounded by a limit cycle appears. In both cases, the eigenvalue close to zero with eigenvector  $u_1$  governs the slow dynamics around these points.

Consider the case of imaginary eigenvalues of the Jacobian,  $\lambda_{\pm} = \sigma \pm i\omega$  with eigenvectors  $v_{\pm} = v_r \pm v_i$ , which satisfy

$$A[v_r v_i] = [v_r v_i] \begin{pmatrix} \sigma & \omega \\ -\omega & \sigma \end{pmatrix}$$

By defining the transformation matrix  $T = [v_r v_i]$ , the linearized matrix is  $Q = T^{-1}AT = \begin{pmatrix} \sigma & \omega \\ -\omega & \sigma \end{pmatrix}$  and the solution of the linear system is of the form

$$e^{At}x_0 = T e^{\sigma t} \begin{pmatrix} \cos(\omega t) & \sin(\omega t) \\ -\sin(\omega t) & \cos(\omega t) \end{pmatrix} T^{-1}x_0$$

By using the coordinate transformation  $u = T^{-1}x$ , we can write the evolution  $\dot{u} = Qu$  with  $u_0 = T^{-1}x_0$ . The linearized dynamic predicts damped oscillations of frequency  $\omega = \sqrt{\det - \frac{Tr^2}{4}}$  when  $\sigma < 0$  and at the Hopf bifurcation point when  $\sigma = 0$  the frequency of oscillations will be  $\omega = \sqrt{\det_H}$ . At the nullcline intersections of linear segments close to the Hopf bifurcation, the oscillation frequency is close to the imaginary part of the eigenvalues:  $\sqrt{\det - \frac{Tr^2}{4}}$ .

Along the slow manifold, the inhibitory and excitatory rates vary linearly as  $I = \frac{a}{b}E \approx \frac{k_{ee}W_{ee}}{k_{ei}W_{ei}}E$ . This relation balances the average current for each population. Therefore, near the BT bifurcation point, the dynamic of slow

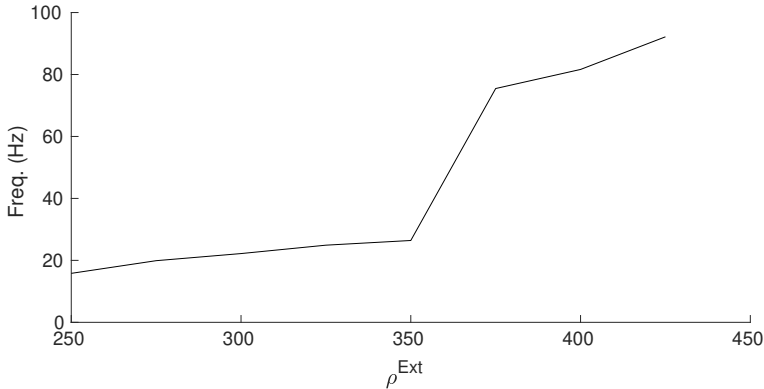


**Fig. 23:** Frequency of avalanches and oscillatory activity increase by input strength. In lower values of excitatory external input, the limit cycle solution is very close to the origin and the system shows avalanches. By increasing the external drive, the limit cycle moves away from the origin (quiescent state) and becomes stable. Oscillations have a higher frequency at higher external input rates with semi-linear relations in both regions.

field,  $E - I$ , can be written as

$$\frac{d(E - I)}{dt} = \epsilon(E - I) + c\left(1 - \frac{a}{b}\right)^{-1}(E - I)^2 \frac{1}{\sqrt{N}} \left(1 - \frac{a}{b}\right)^{\frac{1}{2}} (E + I)^{\frac{1}{2}} \eta(t) \quad (63)$$

where  $\epsilon$  is close to zero, the first nonlinear term of the Taylor expansion has been taken into account and  $\eta(t)$  is a white noise added to the microscopic equation based on the Poisson firing assumption.

### 3.2.6 Characteristics of avalanches

For the values of  $W_{EE}$  near the BT point at the low firing rate, there exists a range of external input strength for which the firing pattern is quasi-periodic with excitatory avalanches followed by inhibitory ones. The mean escape time from the basin of attraction of the quiescent fixed point reduces when the external input increases, and thus, the frequency of avalanches increases. Further increase of external input leads to stability loss of the quiescent state and appearance of higher frequency oscillations in the medium range of rates (see Fig.23).

In the avalanche regime, the membrane potential shows sub-threshold oscillations as can be seen in Fig.20 and Fig.21. In the down phase of the cycle, neurons stay near the resting potential while at the up-state they reside closer to the threshold, but at a distance that permits high variability of firing. The membrane potential of a single neuron is depicted in Fig.24, which shows aperiodic firing and up-down states of membrane potential.

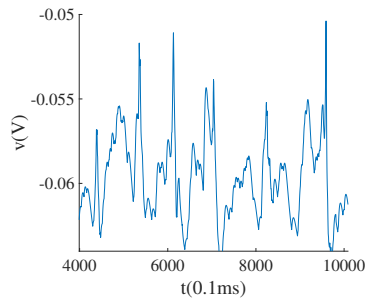


**Fig. 24:** Membrane potential track of a single neuron during avalanche dynamic of Fig.20. Avalanches at population level can be seen as periods of rising potential in the individual neurons which are sustained longer than avalanche range due to slow synaptic decay. Individual neurons do not fire in every single avalanche.

While avalanches occur quasiperiodically, in most of them only a fraction of neurons fire. As shown in (Fig.25D and Fig.26D) neurons fire with CV close to one in the lower  $W_{EE}$  regime, close to the BT point. Variability in the size of avalanches is another interesting item to investigate. The size distribution of avalanches has a longer tail approaching the BT point. It follows a power-law distribution for avalanche size  $P(S) \propto S^{-\tau}$  with slope  $\tau = -1.5$  close to the BT point, see Fig.25A and Fig.26A. Further away from the critical point, avalanches have characteristic average size and their size probability density moves away from the power-law distribution. Furthermore, the probability distribution for the duration of avalanches follows a power law with an exponent close to  $\eta = -2$  near the BT point(see Fig.25B and Fig.26B).

The branching ratio can be defined as the average number of postsynaptic neurons of a specific neuron that fire by receiving the synaptic current from that neuron. The branching ratio can be an indicator of scale-free avalanche dynamics. When inhibition and excitation are balanced and the system resides near a quiescent state, the branching parameter stays close to, but below one which is an indicator of stronger inhibitory feedback. As can be seen in Fig.26 and Fig.27, this value is lower in the parameter regime close to the BT point and becomes  $> 1$  further away from it.

Here, we assume that by synchronous activation of  $n_E$  neurons the postsynaptic neurons which are connected to these neurons will receive both excitatory and inhibitory currents caused by the synchronous input. Each neuron receives a fraction  $k_{EE}$  of excitatory and  $k_{EI}$  of inhibitory currents produced by active neurons. The average potential change among neurons will

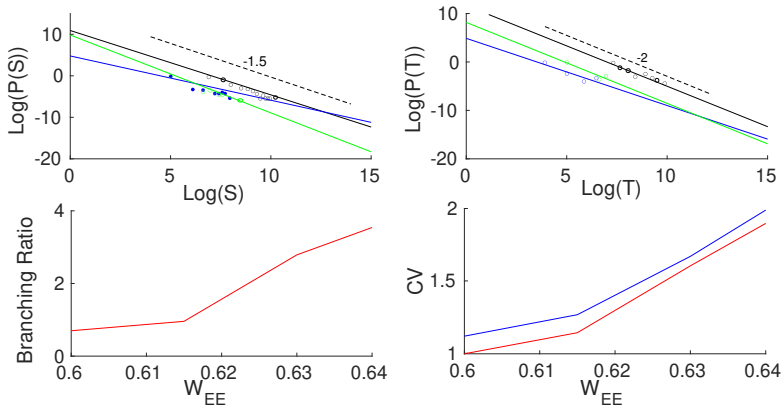


**Fig. 25:** Same as Fig.20 with  $W_{EI} = 2, W_{II} = 2, W_{IE} = 0.75, \rho_{Ext}^{inh} = 150\text{Hz}, \rho_{Ext}^{exc} = 230\text{Hz}$  with different values of  $W_{EE} \in (0.6, 0.65)$ . Avalanche sizes (A) and duration (B) distributions in log-log plot with linear fit. Green line ( $W_{EE} = 0.63$ ), black ( $W_{EE} = 0.615$ ) and blue ( $W_{EE} = 0.6$ ). (C) Branching ratio and (D) CV of firing time intervals of individual neurons (red for the excitatory neurons and blue for the inhibitory ones)

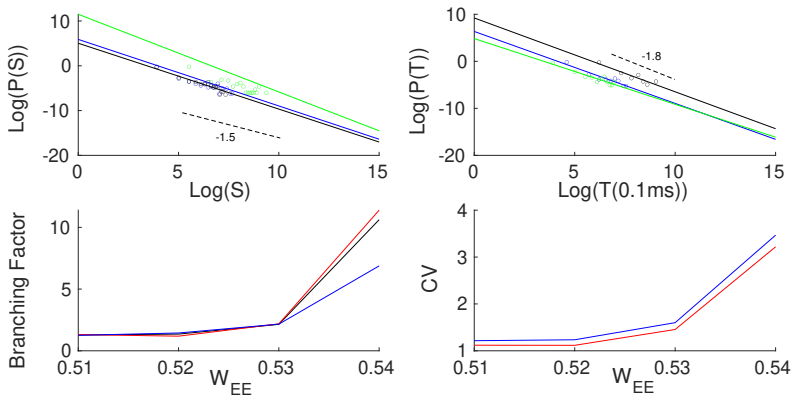


**Fig. 26:** Characteristics of avalanches for the model with  $W_{EI} = 1.5, W_{II} = 2, W_{IE} = 0.75, \rho_{Ext}^{inh} = 150\text{Hz}, \rho_{Ext}^{exc} = 2300\text{Hz}$  and  $W_{EE} \in (0.516, 0.54)$  as in Fig.21. (A-B) Avalanche sizes and duration distributions in log-log plot with their corresponding least square error linear fit. Green line ( $W_{EE} = 0.54$ ), black ( $W_{EE} = 0.53$ ) and blue ( $W_{EE} = 0.51$ ). (C) Branching ratio and (D) CV of interspike time intervals of individual neurons (red for the excitatory neurons and blue for the inhibitory ones).

be

$$\langle \Delta V \rangle = \langle k_{EE} n_E \rangle \frac{1}{C} g_0 w_{EE} \tau (V_{Rexc} - V_E) + \langle k_{EI} n_I \rangle \frac{1}{C} g_0 w_{EI} \tau (V_{Rexc} - V_E) \quad (64)$$

Close to the bifurcation point, there exists a tight dynamic balance between excitatory and inhibitory rates, following Equation 61, which sets  $\langle \Delta V \rangle = 0$ . Based on the assumption that neurons fire with Poisson statistics, we can write the variance of the potential change in the postsynaptic neuron pool as

$$\langle \Delta V^2 \rangle = \tau^2 g_0^2 (\langle k_{EE} n_E \rangle w_{EE}^2 (v_{Rexc} - V_{th})^2 + \langle k_{EI} n_I \rangle (w_{EI})^2 (v_{Rinh} - V_{th})^2) \quad (65)$$

On the other hand, the number of postsynaptic neurons that fire by receiving an increase in voltage of value  $\Delta V$  is

$$\sigma = N_{Exc} \int_{V_{th}-\Delta V}^{V_{th}} P(V, t = \infty) \approx - \frac{N_{exc} \Delta V^2}{2} \frac{\partial p(v^E, t = \infty)}{\partial v} \Big|_{v^E=V_{th}} \quad (66)$$

From equation A1.2 in Appendix .1, for the stationary probability density we have

$$\frac{\partial p(v^E, t = \infty)}{\partial v} \Big|_{v^E=V_{th}} = - \frac{2C^2 \rho_{exc}}{D_e (v_{Rexc} - V_{th})^2 + D_i (v_{Rinh} - V_{th})^2} \quad (67)$$

Inserting Equation 67 in Equation 66 and averaging  $\sigma$  over different realizations of the synchronous firing using Equation 65 and dividing by  $\langle n_E \rangle$  leads to

$$\sigma^E \approx \frac{\tau^2 g_0^2 [w_{EE}^2 \rho_{exc}^{st} (v_{Rexc} - V_{th})^2 + \rho_{exc}^{st} \frac{\langle n_I \rangle}{\langle n_E \rangle} w_{EI}^2 (v_{Rinh} - V_{th})^2]}{D_e (v_{Rexc} - V_{th})^2 + D_i (v_{Rinh} - V_{th})^2} \quad (68)$$

The average number of active inhibitory and excitatory neurons  $\langle n_I \rangle$  and  $\langle n_E \rangle$ , relates to stationary rates as  $\frac{\langle n_I \rangle}{\langle n_E \rangle} = \frac{\rho_I}{\rho_E}$ . Inserting this relation into equation 68, we find out that the branching ratio is close to one near the BT point. Because of slightly stronger inhibitory feedback, it is slightly below one.

Excitatory neurons stay in a low firing regime with average membrane potential close to the middle point between the firing threshold and the resting-state potential, i.e., at  $V \sim -57mv$ . At this point, a sufficient fraction of neurons is close to the threshold, whose activation can cause a series of firing. On the other hand, inhibitory neurons, which have a lower stationary membrane potential because of lower external input, provide negative feedback with a delay that depends on the resting initial state and the strength of the connection between inhibitory and excitatory sub-networks. The dynamic balance

of excitation and inhibition in the linear UP state leads to critical behavior. As average currents to the cells are balanced far from the firing threshold, fluctuations in these currents have a larger effect and therefore, the size of events and their durations are more variable.

Moreover, let us consider the onset of avalanche dynamics in the EI population receiving external input with fixed rates by selecting  $W_{EE}$  as the only dynamic parameter (see Fig.27). By increasing  $W_{EE}$ , a second-order phase transition happens at the Hopf bifurcation. Around this value, the normalized variance of the population rate is maximized and oscillations appear in the system. In Fig.28, this happens at the value  $W_{EE} \approx 0.57$ . Further increase of  $W_{EE}$  results in the saddle-node bifurcation which produces a stable high firing rate state at values around  $W_{EE} \approx 0.67$ .

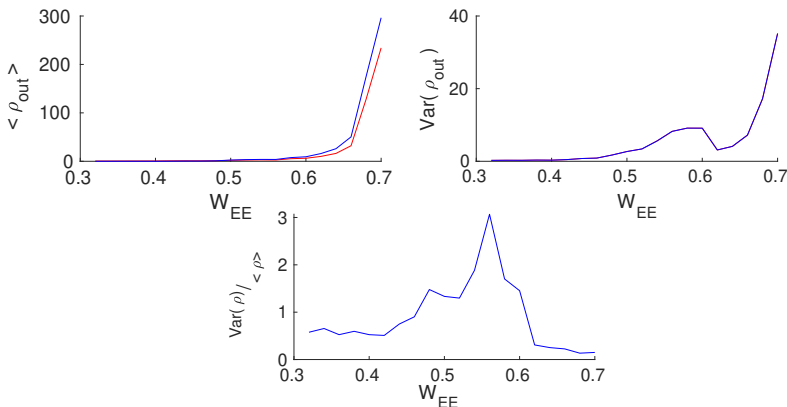


**Fig. 27:** Stationary population rates (A) (Blue for Inh. and Red for Exc.), variance (B) and normalized variance (C) for EI population vs.  $W_{EE}$  at the fixed value of  $\rho_{Ext} = 250Hz$ . Other parameters were set to  $W_{IE} = 0.75$ ,  $\rho_{Inh} = 150Hz$ ,  $W_{II} = W_{EI} = 2$ .

Although the activity is noise-driven, the state of the system depends on synaptic weights, which determine the response to the external input. There must be a self-organizing mechanism, which in a wider range of input strengths and initial configurations of synaptic weights tunes the system close to the BT point.

## 4 Discussion

We have seen that in a large sparse network of spiking neurons the input to the cells in the state of asynchronous firing is Poisson and investigated conditions on Poisson firing at the single neuron level. We chose the conductance-based leaky integrate and fire model to take the strong dependence of the inhibitory

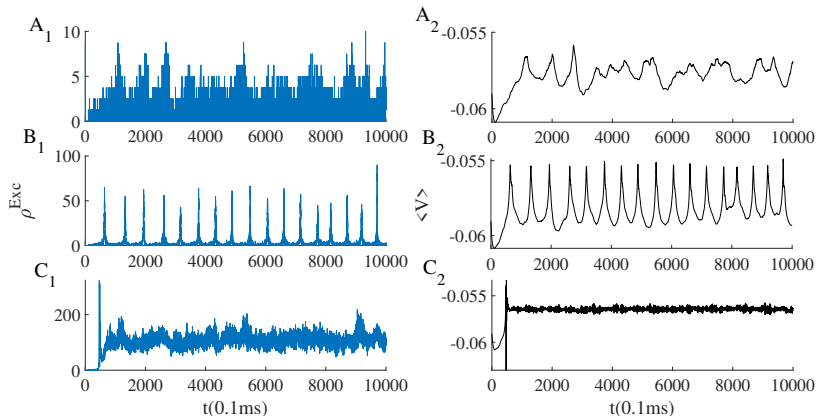


**Fig. 28:** Excitatory population rate (Right plots) and average membrane potential (Left plots) when the system is slightly below the Hopf bifurcation point (A), slightly above Hopf bifurcation point (B), or after the saddle-node bifurcation point (C) corresponding to the states in Fig.27 with the same parameters.

postsynaptic current on the voltage level into consideration. Next, we introduced linearization of the neuron gain function in the Poisson firing regime and presented a linear Poisson neuron model which we used to analyze interconnected networks of excitatory and the inhibitory neurons.

The network of spiking neurons with the assumptions of homogeneity, large size, and sparse connectivity can be modeled by the dynamics of the mean fields. The excitatory and inhibitory mean-field equations are a set of non-linear equations with free parameters including the average synaptic strength between different types of neurons. Taking a set of these free parameters as control parameters of the model one can analyze the bifurcation patterns in the system. Here, we chose the excitatory external drive and the synaptic weight from excitatory to excitatory neurons as control parameters. The latter regulates the strength of the inhibitory feedback in the local population and the former controls the level of forced activity from other populations. The qualitative picture of the bifurcation patterns does not change by the choice of different synaptic weights as control parameter. In analyzing the bifurcation diagram, we are mainly interested in the loss of stability of the quiescent state. This can happen through a saddle-node or a Hopf bifurcation by either increasing the external drive or  $W_{EE}$ . At a certain point called the Bogdanov-Takens point, the saddle-node and Hopf bifurcation lines meet. Near this point there is a tight balance of the inhibitory and the excitatory average currents to the cells. This balance cancels out much of the high amplitude excitatory and inhibitory currents to each cell and causes the average membrane potential of the neurons in the population to stay away from the threshold. In this regime, the activity of the spiking neurons is fluctuation driven which makes the firing

time intervals highly variable. In this case, the statistics of the firing is close to a Poisson point process matching the experimental findings. On the other hand, the balance of excitation and inhibition leads to avalanche style dynamics near the BT point. Slow oscillations emerge at the Hopf bifurcation line and through a saddle-node bifurcation, a pair of low firing stable and unstable fixed points comes into existence.

The next step after identifying the operating dynamical regime that produces the desired output is to investigate mechanisms that can tune the parameters of the system at the desired region of the phase space. The interplay of dynamics and structural organization on different spatiotemporal scales is coordinated and framed by multi-scale self-organization mechanisms that emerged in the organism during evolution. There exist opposing forces that shape the structure and activity such as excitation and inhibition currents produced by excitatory and inhibitory neuron types, depression and potentiation of the connections between neurons, modulation of the concentration of chemicals, and homeostatic considerations on energy consumption and information processing performance. Balancing and coordinating these opposing forces might be one explanation for the scale-free characteristic of spontaneous activity. We shall investigate the self-organization by spike-timing dependent plasticity and short term synaptic depression in another article.

**Acknowledgments.** ME wants to thank International Max Planck Research School for funding his position during the research period.

## Declarations

- Funding: Open access funding provided by Max Planck Society.
- Conflict of interest: The authors declare that the research was conducted in the absence of any commercial or financial relationships that could be construed as a potential conflict of interest.
- Availability of data and materials :The original contributions presented in the study are included in the article/supplementary material, further inquiries can be directed to the corresponding author.
- Code availability :The code used in this work is available for download through github under the following link:
- Authors' contributions:ME and JJ designed research. ME performed research. M.E. wrote the manuscript. J.J. edited the manuscript. All authors reviewed the manuscript, contributed to the article, and approved the submitted version.

## References

- Beggs J, Plenz D (2003) Neuronal avalanches in neocortical circuits. *Journal of Neuroscience* 23:11,167–11,177. <https://doi.org/10.1523/JNEUROSCI.23-35-11167>



- Benayoun M, Cowan J, van Drongelen W, et al (2010) Avalanches in a stochastic model of spiking neurons. *PLoS Comput Biol* 6(7). <https://doi.org/10.1371/journal.pcbi.1000846>
- Bornholdt S, Roehl T (2003) Self-organized critical neural networks. *Phys Rev E* 67 78:74–80. <https://doi.org/10.1007/s001090000086>
- Bressloff P (2011) Spatiotemporal dynamics of continuum neural fields. *Journal of Physics A: Mathematical and Theoretical* 45. <https://doi.org/10.1088/1751-8113/45/3/033001>
- Brochini L, Costa A, Abadi M, et al (2016) Phase transitions and self-organized criticality in networks of stochastic spiking neurons. *Scientific Reports* volume 6 <https://doi.org/10.1038/srep35831>
- Brunel N, Hakim V (1999) Fast global oscillations in networks of integrate-and-fire neurons with low firing rates. *Neural Comput* 11(7):1621–71. <https://doi.org/10.1162/089976699300016179>.
- Brunel N, Hakim V (2000) Dynamics of sparsely connected networks of excitatory and inhibitory spiking neurons. *J Comput Neurosci* 8:183–208. <https://doi.org/10.1023/A:1008925309027>
- Brunel N, Hakim V (2008) Sparsely synchronized neuronal oscillations. *Chaos* 18. <https://doi.org/10.1063/1.2779858>
- Cowan D, Neuman J, Kiewiet B, et al (2013) Self-organized criticality in a network of interacting neurons. *J Stat Mech* <https://doi.org/10.1088/1742-5468/2013/04/P04030>
- Ehsani M, Jost J (2022) Self organized criticality in a mesoscopic model of excitatory-inhibitory neuronal populations by short-term and long-term synaptic plasticity[pre-print]. *Arxiv* <https://doi.org/http://arxiv.org/abs/2203.07841>.
- Ermentrout B (1998) Neural networks as spatio-temporal pattern-forming systems. *Rep Prog Phys* 61
- Friedman N, Ito S, Brinkman A, et al (2012) Universal critical dynamics in high resolution neuronal avalanche data. *Phys Rev Lett* 108. <https://doi.org/10.1103/PhysRevLett.108.208102>.
- Gong P, Nikolaev A, van Leeuwen C (2003) scale-invariant fluctuations of the dynamical synchronization in human brain electrical activity. *Neuroscience Letters*, 336. [https://doi.org/10.1016/s0304-3940\(02\)01247-8](https://doi.org/10.1016/s0304-3940(02)01247-8).

- Hahn G, Petermann T, Havenith M, et al (2010) Neuronal avalanches in spontaneous activity in vivo. *Neurophysiol* 104(6):3312–22. <https://doi.org/10.1152/jn.00953.2009>
- Haider B, Duque A, Hasenstaub A, et al (2006) Neocortical network activity in vivo is generated through a dynamic balance of excitation and inhibition. *The Journal of Neuroscience* 26(17):4535–4545. <https://doi.org/10.1523/JNEUROSCI.5297-05.2006>
- Kistler W, van Hemmen J (2000) Modeling synaptic plasticity in conjunction with the timing of pre- and postsynaptic action potentials. *Neural Comput* 12(2):385–405 doi: 101162/089976600300015844 PMID: 10636948
- Klaus A, Yu S, Plenz D (2011) Statistical analyses support power law distributions found in neuronal avalanches. *PLoS One* 6(5). <https://doi.org/10.1371/journal.pone.0019779>
- Levina A, Herrmann J, Geisel T (2007) Dynamical synapses causing self-organized criticality in neural networks. *Nature Physics* volume 3. <https://doi.org/10.1038/nphys758>
- Levina A, Herrmann J, Geisel T (2009) Phase transitions towards criticality in a neural system with adaptive interactions. *Physical Review Letters* 102. <https://doi.org/10.1103/PhysRevLett.102.118110>
- Mazzoni A, Broccard F, Garcia-Perez E, et al (2007) On the dynamics of the spontaneous activity in neuronal networks. *PLoS one* 2(5). <https://doi.org/10.1371/journal.pone.0000439>
- Meisel C, Gross T (2009) Adaptive self-organization in a realistic neural network model. *Physical Review E* 80 102. <https://doi.org/10.1103/PhysRevE.80.061917>
- Meisel C, Olbrich E, Shriki O, et al (2013) Fading signatures of critical brain dynamics during sustained wakefulness in humans. *Journal of Neuroscience* <https://doi.org/10.1007/s001090000086>
- Okun M, Lampl I (2008) Instantaneous correlation of excitation and inhibition during ongoing and sensory-evoked activities. *Nat Neurosci*, 11:535–537. <https://doi.org/10.1038/nn.2105>
- Peng J, Beggs J (2013) Attaining and maintaining criticality in a neuronal network model. *Physica A: Statistical Mechanics and its Applications* <https://doi.org/10.1016/j.physa.2012.11.013>
- Petermann T, Thiagarajan T, Lebedev M, et al (2009) Spontaneous cortical activity in awake monkeys composed of neuronal avalanches. *PNAS*

106(37):15,921–15,926. <https://doi.org/10.1073/pnas.0904089106>

Raichle M (2010) Two views of brain function. *Trends Cogn Sci* 14:180–190. <https://doi.org/10.1016/j.tics.2010>

Ribeiro T, Copelli M, Caixeta F, et al (2010) Spike avalanches exhibit universal dynamics across the sleep-wake cycle. *PLoS ONE* 5(11). <https://doi.org/10.1371/journal.pone.0014129>

Rybarsch M, Bornholdt S (2014) Avalanches in self-organized critical neural networks: A minimal model for the neural soc universality class. *PLoS ONE* 9(4). <https://doi.org/10.1371/journal.pone.0093090>

di Santo S, Villegas P, Burioni R, et al (2018) Landau–ginzburg theory of cortex dynamics: Scale-free avalanches emerge at the edge of synchronization. *PNAS* 115(7):E1356–E1365. <https://doi.org/10.1073/pnas.1712989115>

Shu Y, Hasenstaub A, McCormick D (2003) Turning on and off recurrent balanced cortical activity. *Nature* 423:288–293. <https://doi.org/10.1038/nature01616>

Siebert A (1951) On the first passage time probability problem. *Phys Rev* 81. <https://doi.org/10.1103/PhysRev.81.617>

Softky W, Koch C (1993) The highly irregular firing of cortical cells is inconsistent with temporal integration of random epsps. *The Journal of Neuroscience* 13(1):334–50. <https://doi.org/10.1523/JNEUROSCI.13-01-00334.1993>.

Takeda Y, Hiroe N, Yamashita O, et al (2016) Estimating repetitive spatiotemporal patterns from resting-state brain activity data. *Neuroimage* 133:251–265. <https://doi.org/10.1016/j.neuroimage.2016.03.014>

Thompson G, Pan W, ME. M, et al (2014) Quasiperiodic patterns (qpp): Large-scale dynamics in resting state fmri that correlate with local infraslow electrical activity. *Neuroimage* 84:1018–1031. <https://doi.org/10.1016/j.neuroimage.2014>

## .1 Gaussian approximation for response to the Poisson input

The Fokker-Planck equation corresponding to Eq.18 in section 3.1 in the Itô interpretation is

$$\begin{aligned} \frac{\partial p(v, t)}{\partial t} = & -\frac{1}{C} \frac{\partial}{\partial v} [(a - bv)p(v, t)] + \frac{1}{C^2} \frac{D_e}{2} \frac{\partial^2}{\partial v^2} (v_{Rexc} - v(t))^2 p(v, t) \\ & + \frac{1}{C^2} \frac{D_i}{2} \frac{\partial^2}{\partial v^2} (v_{Rinh} - v(t))^2 p(v, t) \equiv -\frac{\partial}{\partial v} J(v, t) \end{aligned} \quad (\text{A1.1})$$

with the boundary condition  $p(V_{th}, t) = 0$ . The density current at  $v = V_{th}$  is equivalent to the firing rate, and this current is fed back to the equation at  $v = V_r$  resulting in a discontinuity of the membrane potential derivative.

$$J(v_r^+, t) - J(v_r^-, t) = J(v_{th}, t - t_{ref}) \equiv r(t - t_{ref})$$

The stationary probability distribution and firing rate are obtained by solving the equation

$$J_{st}(v) = r_0 \Theta(v - V_r)$$

which results in

$$\begin{aligned} & \frac{1}{C} \left\{ a - bv + \frac{1}{C} D_e (v_{Rexc} - v) + \frac{1}{C} D_i (v_{Rinh} - v) \right\} p(v) \\ & - \frac{1}{C^2} \left\{ \frac{D_e}{2} (v_{Rexc} - v)^2 + \frac{D_i}{2} (v_{Rinh} - v)^2 \right\} \frac{dp(v)}{dv} = r \end{aligned} \quad (\text{A1.2})$$

for  $V_r < v < V_{th}$ . Together with the normalization requirement  $\int_{-\infty}^{V_{th}} p(v) dv + r_0 * t_{ref} = 1$  one can solve equation A1.2. numerically for both the stationary probability distribution and the stationary firing rate.

When  $V_{st}$  is sufficiently smaller than  $V_{th}$ , i.e., in the low firing rate regime, we can ignore the non-linearity caused by the threshold and write down the evolution of the mean and variance of the membrane potential as follows (See Fig.A1.1)

$$\begin{aligned} \frac{d\langle v(t) \rangle}{dt} &= \frac{1}{C} (a - b\langle v(t) \rangle) \\ \frac{d\text{Var}(v, t)}{dt} &= -\frac{2b}{C} \text{Var}(v, t) + \frac{1}{C^2} [D_e \langle (V_{Rexc} - v(t))^2 \rangle + D_i \langle (v(t) - V_{Rinh})^2 \rangle] \\ &= \left( -\frac{2b}{C} + \frac{D_e + D_i}{C^2} \right) \text{Var}(v, t) + \frac{1}{C^2} [D_e (V_{Rexc} - \langle v \rangle)^2 + D_i (V_{Rinh} - \langle v \rangle)^2] \end{aligned}$$

This leads to the stationary value for average and variance of the membrane voltage

$$\begin{aligned}\langle v \rangle_{st} &= \frac{a}{b} \\ \text{Var}(v)_{st} &= \frac{1}{2bC - (D_e + D_i)} [D_e (V_{Rexc} - \langle v \rangle_{st})^2 + D_i (\langle v \rangle_{st} - V_{Rinh})^2]\end{aligned}\tag{A1.3}$$

In the low firing regime, the stationary probability distribution can be approximated as (see Fig.A1.2):

$$\begin{aligned}P_{st}(V) &= \frac{1}{\sqrt{2\pi}\sigma_{V(st)}} \exp\left(-\frac{(V - \langle V \rangle)^2}{2\sigma^2}\right) \\ &\quad + c\delta(V - V_{Rest}) \quad V < V_{th} \\ P_{st}(V) &= 0 \quad V \geq V_{th}\end{aligned}$$

The stationary firing rate is derived from equation A1.2 by plugging in the Gaussian approximation for the stationary potential probability density  $P(V, t \rightarrow \infty) = N(\langle V \rangle, \sigma_{V(st)})$ :

$$\begin{aligned}r &= \frac{1}{C^2} \frac{1}{2} D(V_{th})^2 \frac{dp(V)}{dV} \Big|_{V=V_{th}} \\ &= -\frac{b}{C} \frac{D(V_{th})^2}{D(\langle V \rangle)^2} * \frac{(V_{th} - \langle V \rangle)}{\sigma_{V(st)}\sqrt{2\pi}} \exp\left(-\frac{(V_{th} - \langle V \rangle)^2}{2\sigma_{V(st)}^2}\right) \\ &\approx \frac{b}{\sqrt{\pi}C} \frac{(V_{th} - \langle V \rangle)}{\sqrt{2}\sigma_{V(st)}} \left(1 - \frac{(V_{th} - \langle V \rangle)^2}{2\sigma_{V(st)}^2}\right)\end{aligned}\tag{A1.4}$$

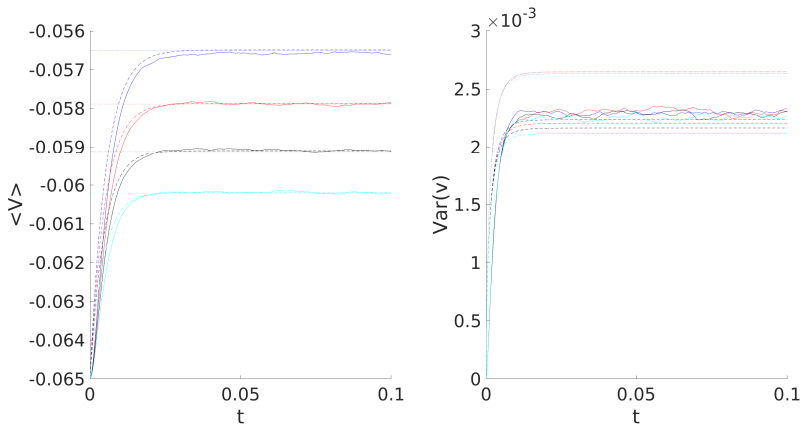
## .2 Tau expansion

The equation  $\frac{dv(t)}{dt} = f(v) + \eta(t)g(v)$  where  $\eta(t)$  is colored Gaussian noise with correlation

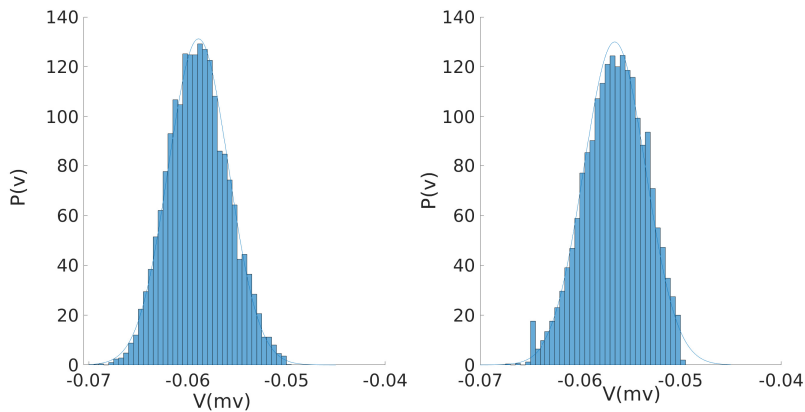
$$\langle \eta(t)\eta(t') \rangle = \frac{H}{\tau} e^{-\frac{(t-t')}{\tau}}$$

corresponds to the following Fokker-Planck equation derived by expansion with respect to  $\tau$  :

$$\frac{\partial p(v, t)}{\partial t} = -\frac{\partial}{\partial v} [f(v)p(v, t)] + H \frac{\partial}{\partial v} g(v) \frac{\partial}{\partial v} \left\{ g(v) \left[ 1 + \tau g(v) \left( \frac{f(v)}{g(v)} \right)' \right] p(v, t) \right\}$$

**Fig. A1.1**

**Fig. A1.1:** Evolution of the mean and the variance of the potential distribution of a population of neurons each receiving a fixed equal inhibitory input rate but different excitatory rates. Dashed lines are the trajectories determined from Gaussian noise approximation and the dotted lines are derived from the tau expansion method. The approximation by tau expansion improves the estimation of variance. ( $\tau_{syn} = 2.5ms$ )

**Fig. A1.2**

**Fig. A1.2:** Membrane potential distribution and Gaussian approximation (Blue lines) for two different sets of inhibitory and excitatory Poisson inputs. The average membrane potential values are  $-0.59mv$ (Left) and  $-0.56mv$ (Right)

$$\begin{aligned}
&= -\frac{\partial}{\partial v}[(f(v) + Hg(v)g'(v))p(v, t)] + H\frac{\partial^2}{\partial v^2}\{g(v)^2p(v, t)\} \\
&\quad - \tau H\frac{\partial}{\partial v}\{g'(v)(g(v)f'(v) - g'(v)f(v))P(v, t)\} \\
&\quad + \tau H\frac{\partial^2}{\partial v^2}\{g(v)(g(v)f'(v) - g'(v)f(v))p(v, t)\}
\end{aligned}$$

In our case  $H_e = \frac{\tau^2 g_0^2 w_e^2 \lambda_e}{2} = \frac{D_e}{2}$ , resulting in:

$$\begin{aligned}
\frac{\partial p(v, t)}{\partial t} &= -\frac{1}{C}\frac{\partial}{\partial v}\{(a - bv + F(v))p(v, t)\} \\
&\quad + \frac{D_e}{2C^2}\frac{\partial^2}{\partial v^2}\{G_e(v)p(v, t)\} + \frac{D_i}{2C^2}\frac{\partial^2}{\partial v^2}\{G_i(v)p(v, t)\} \quad (\text{A2.1})
\end{aligned}$$

where

$$\begin{aligned}
F(v) &= \frac{D_e}{2C}[-2(v_{Rexc} - v(t)) - \frac{\tau}{C}(a - bV_{Rexc})] \\
&\quad + \frac{D_i}{2C}[-2(v_{Rinh} - v(t)) - \frac{\tau}{C}(a - bV_{Rinh})] \\
G_e(v) &= (v_{Rexc} - v(t))^2 + \frac{\tau}{C}(v_{Rexc} - v(t))(a - bV_{Rexc}) \\
G_i(v) &= (v_{Rinh} - v(t))^2 + \frac{\tau}{C}(v_{Rinh} - v(t))(a - bV_{Rinh})
\end{aligned}$$

### 3 Neuron response in higher values of input rates and synaptic time constant

As it can be seen from Fig.A1.1 and Fig.3C in section 3.1, the stationary standard deviation of the membrane potential in the case of Poisson input does not show high sensitivity to input rates when the stationary mean potential is fairly away from the threshold. In Fig.3, increasing the excitatory input rate by 60% causes a 2% increase of  $\sigma(V)_{st}$  on average for different values of  $\langle v \rangle_{st}$ . This can be predicted from equation A1.3 as both the input noise and drift term in the numerator and the denominator depend linearly on input rates. Suppose  $\langle v \rangle_{st}$  is fixed for a set of inhibitory and excitatory rates, which means there is a linear relation of the form  $\rho_E = \kappa\rho_I + c$  originating from the condition on the fixed stationary average membrane potential. In the limit of high rates, the stationary variance approaches a constant value:

$$Var(v)_{st} = \frac{\sigma^2}{2bC} = \frac{\alpha - \frac{\beta}{\lambda_E}}{\gamma - \frac{\eta}{\lambda_E}}$$

$$\frac{\alpha}{\gamma} = \frac{\tau g_0 (V_{Rexc} - \langle V_{st} \rangle) (\langle V_{st} \rangle - V_{Rinh})}{V_{Rexc} - V_{Rinh}} * [w_E (V_{Rexc} - \langle V_{st} \rangle) + w_I (\langle V_{st} \rangle - V_{Rinh})]$$

$$\frac{\beta}{\eta} = \frac{w_i \tau g_0 (\langle V_{st} \rangle - V_{Leak}) (\langle V_{st} \rangle - V_{Rinh})^2}{\langle V_{st} \rangle - V_{Leak}} = w_i \tau g_0 (\langle V_{st} \rangle - V_{Rinh})^2 \quad (\text{A3.1})$$

when  $\frac{\alpha}{\gamma} > \frac{\beta}{\eta}$ , the variance of the stationary membrane potential (and hence also the output rate) increases by proportional increase of both inhibitory and excitatory rates and reaches a constant value  $\frac{\alpha}{\gamma}$ . This condition translates into  $w_E (V_{Rexc} - \langle V_{st} \rangle)^2 > w_I (V_{Rinh} - \langle V_{st} \rangle)^2$ . As long as  $\langle V_{st} \rangle$  is adequately lower than  $V_{th}$ ,  $w_E (V_{Rexc} - \langle V_{st} \rangle) \approx w_I (V_{Rinh} - \langle V_{st} \rangle)$  and the condition mentioned above holds because  $(V_{Rexc} - \langle V_{st} \rangle)$  is greater than  $(V_{Rinh} - \langle V_{st} \rangle)$  by a factor of about 2.

We remind the reader that the Gaussian approximation is only legitimate in the case of small  $\tau$  and for a low firing rate regime. We want to consider cases in which these two conditions are not satisfied. Firstly, at higher values of  $\tau_{syn}$  and at the stationary values of the average membrane potential lower than the threshold (low firing regime), there is an inversion of the mentioned scenario. In this case, at sufficiently high values of the input rates, conditioned on constant average membrane potential, the variance of the membrane potential and accordingly the output rate decrease (Fig.3A). This is due to the filtering effect of the input by the gradual decay of the synaptic conductances. Using the method of  $\tau$ -expansion of Appendix.2, we will consider autocorrelation in synaptic conductance and partially take into account this effect. The filtering of the high-frequency signal by the slow conductances is a mechanism of gain control. In general, the decay and the rise time of the inhibitory synapses are longer than the excitatory ones which would highlight the inhibitory input as its overall strength increases through temporal persistence. In addition, the voltage-dependent inhibitory current is higher at higher values of the membrane potential. The balanced average membrane potential is somewhere in the mid-range. Longer synaptic decay time constant, higher synaptic strength, delay, and potential dependence of the inhibitory synapses increase the overall inhibition strength and compensate for the smaller number of them in comparison with excitatory synapses. It should be noted that output rates on the constant voltage level line with balanced input at  $V = -57mv$  vary linearly with the input rates at moderate rate values corresponding to the low firing rate regime (Fig.3A).

On the other hand, when the stationary average membrane potential is located right at the threshold value, in conflict with the low firing regime assumption, equation A3.1 does not hold and higher rates of balanced input lead to a higher output rate independent of the value of  $\tau_{syn}$  (Fig.3B). Moreover, the output rate varies like  $\sqrt{I_{in}}$ . For analyzing the low firing rate, we could linearize the output rate around the midpoint of the neuron potential range, i.e., at  $V = -57mv$ .



#### .4 First passage time

To determine first passage time(FPT) statistics let us first review the recursive formula for FPT moments as discussed in Siegert [Siegert \(1951\)](#). Suppose the stochastic process  $X_t$  with conditional probability density  $P(x, t | x_0)$  satisfies the Fokker-Planck equation

$$\frac{\partial p(x, t | x_0)}{\partial t} = -\frac{\partial}{\partial x}[A(x)p(x, t | x_0)] + \frac{1}{2} \frac{\partial^2}{\partial x^2}(B(x)p(x, t | x_0))$$

with initial and boundary conditions  $P(x, t_0 | x_0) = \delta(x - x_0)$  and  $P(\pm\infty, t | x_0) = 0$ , respectively. The first passage time probability density  $\rho(\Theta | t, x_0)$  of the stochastic process following the above Fokker-Planck equation satisfies

$$\rho(\Theta | t, s) = -2 \frac{\partial}{\partial t} \int_{-\infty}^s P(\Theta, t | y) dy$$

Based on this equation we can write a recursion formula for moments of FPT with diffusion strength  $B(y)$  and drift term  $A(y)$ :

$$t_n(\Theta | x_0) = n \int_{x_0}^{\Theta} \frac{2dz}{B(z)W(z)} \int_{-\infty}^z W(k)t_{n-1}(\Theta | k)dk \quad (\text{A4.1})$$

with  $t_0 = 1$ , and  $W(k)$  is the stationary probability distribution

$$W(k) = \frac{C}{B(x)} \exp\left[\int dx \frac{2A(x)}{B(x)}\right] \quad (\text{A4.2})$$

In particular, for the first moment we have

$$t_1(\Theta | x_0) = \int_{x_0}^{\Theta} \frac{2dz}{B(z)W(z)} \int_{-\infty}^z W(x)dx \quad (\text{A4.3})$$

For the case of Langevin equation in section [3.1.1](#), writing  $x_0 = (V_{leak} - V_{th}) + (V_{th} - \frac{a}{b}) = -\Theta + x_{th}$  and using equations [A4.2](#) and [A4.3](#), the average first passage time can be written as

$$\begin{aligned} t_1(x_{th} | x_0) &= \frac{\sqrt{\pi}}{b} \int_{x_0 \sqrt{\frac{b}{\sigma^2}}}^{x_{th} \sqrt{\frac{b}{\sigma^2}}} \sqrt{\frac{b}{\sigma^2}} e^{z^2} (1 + erf(z)) \\ &= \frac{\sqrt{\pi}}{b} \left[ \int_0^{x_{th}} \sqrt{\frac{b}{\sigma^2}} e^{z^2} (1 + erf(z)) \right] \end{aligned}$$

$$- \int_0^{(-\Theta+x_{th})\sqrt{\frac{b}{\sigma^2}}} \sqrt{\frac{b}{\sigma^2}} e^{z^2} (1 + \operatorname{erf}(z))]$$

where  $\operatorname{erf}(\cdot)$  is the Gauss error function.

Taking  $y = x_{th}\sqrt{\frac{b}{\sigma^2}}$  and  $\theta = \Theta\sqrt{\frac{b}{\sigma^2}}$  and using the following series expansion for small  $y$

$$\begin{aligned} \int_0^y e^{z^2} dz &= y + \frac{y^3}{3} + \frac{y^5}{10} \dots \\ \int_0^y e^{z^2} \operatorname{erf}(z) dz &= \frac{1}{\sqrt{\pi}} (y^2 + \frac{y^4}{3} + \frac{4y^6}{45} \dots) \\ \int_0^{-\theta+y} e^{z^2} (1 + \operatorname{erf}(z)) dz &= \int_0^{-\theta} e^{z^2} (1 + \operatorname{erf}(z)) dz + y(e^{-\theta^2} (1 + \operatorname{erf}(-\theta))) \\ &\approx \int_0^{-\theta} e^{z^2} (1 + \operatorname{erf}(z)) dz \equiv \kappa \end{aligned} \tag{A4.4}$$

we arrive at equation 20 of section 3.1.1.

It can be seen from equation A3.1 that the factor  $\sqrt{\frac{b}{\sigma^2}}$  in large balanced rates of excitatory and inhibitory inputs asymptotically approaches a constant value. Therefore, we can approximate  $\kappa$  to be very weakly dependent on input rates and take it as a constant factor. Next, we want to investigate the variance of first passage time. From the recursion formula ?? we have

$$t_2(x_{th} | x_0) = \frac{2\pi}{b^2} \int_{-\infty}^{x_{th}\sqrt{\frac{b}{\sigma^2}}} \sqrt{\frac{b}{\sigma^2}} e^{z^2} (1 + \operatorname{erf}(z))^2 \int_z^{x_{th}\sqrt{\frac{b}{\sigma^2}}} \sqrt{\frac{b}{\sigma^2}} dr e^{r^2} \Theta(r - x_0\sqrt{\frac{b}{\sigma^2}})$$

After some straightforward calculations we arrive at

$$\begin{aligned} t_2(x_{th} | x_0) &= \frac{2\sqrt{\pi}}{b} t_1(x_{th} | x_0) \left[ \int_0^{x_{th}\sqrt{\frac{b}{\sigma^2}}} \sqrt{\frac{b}{\sigma^2}} e^{z^2} (1 + \operatorname{erf}(z)) \right] \\ &\quad + \frac{2\sqrt{\pi}}{b^2} \ln(2) \left[ \int_0^{x_{th}\sqrt{\frac{b}{\sigma^2}}} \sqrt{\frac{b}{\sigma^2}} e^{z^2} - \int_0^{x_0\sqrt{\frac{b}{\sigma^2}}} \sqrt{\frac{b}{\sigma^2}} e^{z^2} \right] \\ &\quad - \frac{2\sqrt{\pi}}{b^2} \left[ \phi(x_{th}\sqrt{\frac{b}{\sigma^2}}) - \phi(x_0\sqrt{\frac{b}{\sigma^2}}) \right] \\ &\quad - \frac{2\sqrt{\pi}}{b^2} \left[ \psi(x_{th}\sqrt{\frac{b}{\sigma^2}}) - \psi(x_0\sqrt{\frac{b}{\sigma^2}}) \right] \end{aligned}$$

where functions  $\phi$  and  $\psi$  are multi-variable integrals containing powers of  $erf$  and  $e^{x^2}$  in the integrand with series expansion :

$$\phi(y) = \sum_{n=0}^{\infty} \frac{y^{2n+3}}{(n+1)!(2n+3)} \sum_{k=0}^n \frac{1}{2k+1}$$

$$\psi(y) = \sum_{n=0}^{\infty} \frac{2^n y^{2n+4}}{(n+2)(2n+3)!!} \sum_{k=0}^n \frac{1}{k+1}$$

Rewriting the first term in brackets in terms of first passage time and considering just terms linear in  $x_{th}$

$$\begin{aligned} t_2(x_{th} | x_0) &= 2t_1(x_{th} | x_0)[t_1(x_{th} | x_0) \\ &+ \frac{\sqrt{\pi}}{b} \int_0^{(-\Theta+x_{th})} \sqrt{\frac{b}{\sigma^2}} e^{z^2} (1 + erf(z))] \\ &+ \frac{2\sqrt{\pi}}{b^2} \ln(2) \left[ \int_0^{x_{th}} \sqrt{\frac{b}{\sigma^2}} e^{z^2} - \int_0^{x_0} \sqrt{\frac{b}{\sigma^2}} e^{z^2} \right] \\ &- \frac{2\sqrt{\pi}}{b^2} \left[ \phi\left(x_{th} \sqrt{\frac{b}{\sigma^2}}\right) - \phi\left(x_0 \sqrt{\frac{b}{\sigma^2}}\right) \right] \\ &- \frac{2\sqrt{\pi}}{b^2} \left[ \psi\left(x_{th} \sqrt{\frac{b}{\sigma^2}}\right) - \psi\left(x_0 \sqrt{\frac{b}{\sigma^2}}\right) \right] \\ &\approx 2t_1(x_{th} | x_0)^2 + \frac{2x_{th}\sqrt{\pi}}{b\sqrt{b}\sigma} \ln(2) \\ &+ C(x_{th} = 0) \end{aligned} \tag{A4.5}$$

where the constant  $C$ , coming from the integral, is negative.